Structural and magnetic properties of MnCoGe ferromagnetic thin films produced by reactive diffusion

E. Assaf, A. Portavoce, L. Patout, M. Bertoglio, R. Clerac, K. Hoummada, A. Charai, S. Bertaina

Structural and magnetic properties of MnCoGe ferromagnetic thin films produced by reactive diffusion

E. Assaf[1], A. Portavoce[2,*], L. Patout[2], M. Bertoglio[2], R. Clérac[3,4], K. Hoummada[1], A. Charaï[1], and S. Bertaina[2]

[1]*Aix-Marseille University, IM2NP, Faculté des Sciences de Saint-Jérôme case 142, 13397 Marseille, France*
[2]*CNRS, IM2NP, Faculté des Sciences de Saint-Jérôme case 142, 13397 Marseille, France*
[3]*CNRS, CRPP, UPR 8641, 33600 Pessac, France*
[4]*Univ. Bordeaux, CRPP, UPR 8641, 33600 Pessac, France*

ABSTRACT

The structure, the chemistry, and the magnetic properties of MnCoGe thin films elaborated by reactive diffusion were investigated. In situ X-ray diffraction (XRD) was used to study phase formation during thin film reaction. Mn-Co, Mn-Ge, and Co-Ge binary systems were studied before investigating phase formation during Mn-Ge-Co ternary system reaction. Three pure layers of Mn, Ge, and Co were successively deposited by magnetron sputtering on SiO_2 to form a 200 nm-thick Co/Ge/Mn stack, and annealed. Six phases were observed during reaction, first following the sequential phase formation observed for the binary systems at the two Mn/Ge and Ge/Co interfaces, and ending with the formation of a single ternary compound MnCoGe at 673 K. The structure and the composition of the MnCoGe films were characterized using XRD, atomic force microscopy, transmission electron microscopy, and energy dispersive X-ray spectroscopy. The magnetic properties of the films were studied using superconducting quantum interference device (SQUID) and ferromagnetic resonance (FMR) measurements. The obtained MnCoGe thin films are polycrystalline with the stoichiometric composition Mn:Co:Ge(1/3:1/3:1/3), and show high porosity. They are made of grains exhibiting both the Ni_2In-type hexagonal structure and the TiNiSi-type orthorhombic structure.

Keywords: MnCoGe, Thin films, Reactive diffusion, Ferromagnetic.

*Corresponding author: alain.portavoce@im2np.fr

1. Introduction

In addition to the continuous development of micro- and opto-electronics, recent technologies or phenomena involving electron spin, such as spintronics [1-3] and spin-caloritronics [4-8], are expected to allow new types of devices to be produced [9-14] for innovative applications such as energy harvesting [5-6,11, 15-18]. For example, spintronics aims to produce new logical devices and memories [1-2,19-20], while spin-caloritronics should provide solid-state magnetic refrigeration devices [7-8, 21-23] and spin-thermoelectric devices [11,15,18,24]. The development of these technologies is based on the use of ferromagnetic materials. Among them, ferromagnetic metal-semiconductor compounds and alloys can present interesting benefits, such as the possibility of being integrated in already-developed technologies based on the considered semiconductor [25-31], and of providing a high-quality contact on the semiconductor [26, 28, 32]. Silicides and germanides are commonly used to build ohmic contacts on Si, Ge and their alloy SiGe in complementary metal-oxide-semiconductor (CMOS) technology [33-35]. Thus, ferromagnetic silicides and germanides should be easily integrated in CMOS processes, allowing the industrial production of reliable highly-integrated devices at a reasonable cost. In addition, silicides and germanides are generally considered to be environmentally-friendly materials. Portable applications require the use of nanostructures based on thin films or 1D and 0D objects such as wires and islands. However, despite their interesting potential for mobile applications, a significant number of ferromagnetic germanides were only studied to date in their bulk state, such as Heusler alloys for example [17,36]. Thin films may exhibit properties other than those of relaxed bulk materials, especially since their structure,

composition, and stress state can vary depending on the fabrication method and the substrate material used.

For example, promising Ge-based spintronic technology [37] is still looking for spin injector and detector solutions. Room temperature (RT) injection of significant spin-polarized current in semiconductors using metallic ferromagnetic contacts is possible if the contact exhibits: i) a high Curie temperature (T_C > RT), ii) significant spin polarization, iii) a resistivity close to the semiconductor resistivity, iv) a large spin-flip length, and v) whether this contact can be grown on the semiconductor as a thin film. C-doped Mn_5Ge_3 thin films [38-30] are currently investigated as metallic ferromagnetic contacts for Ge-based spintronics [37]. However, the need to dope the germanide films with C in order to reach a T_C larger than 400 K can be limiting for industrial applications, due to possible undesirable C contaminations. MnCoGe and MnCoGe-based alloys are generally studied for their magnetocaloric properties. However, the MnCoGe compound possesses interesting properties that could also be of interest for metallic ferromagnetic contact production on Ge. For example, like Mn_5Ge_3, MnCoGe is compatible with current microelectronic industrial production processes [27]. Furthermore, the T_C of undoped MnCoGe in its RT-stable orthorhombic structure is about 60 K higher than the T_C of Mn_5Ge_3, and was shown to increase to similar T_C as C-doped Mn_5Ge_3 using less detrimental dopants such as Si [8]. In addition, its resistivity is expected to be similar to Mn_5Ge_3 resistivity (~ 300 μΩ cm at 300 K), which is close to doped Ge [28].

This work focuses on ferromagnetic MnCoGe thin film production using magnetron sputtering deposition and reactive diffusion (RD), which are classically used in the 'Salicide' process [33] allowing for contact fabrication in CMOS technology. Bulk MnCoGe compound presents a structural-phase transition between a low-temperature ferromagnetic TiNiSi-type

orthorhombic phase (space group *Pnma*) and a high-temperature paramagnetic Ni_2In-type hexagonal phase (space group $P6_3/mmc$) occurring at T_t ~ 420 K [7-8,23,39-41]. Furthermore, the magnetic transition between the ferromagnetic and the paramagnetic states takes place at T_c ~ 275 K for the hexagonal austenite phase (Hexa-MnCoGe) and at T_c ~ 355 K for the orthorhombic martensite phase (Ortho-MnCoGe) [7-8,23,39,41]. According to the literature, the magnetic and the structural transition temperatures in bulk MnCoGe can be modified to coincide by i) modifying the Mn and Co stoichiometry in the compound, such as in $Mn_{1-x}CoGe$ [42] and $Mn_{1+x}Co_{1-x}Ge$ [43], ii) alloying MnCoGe with a fourth element, such as in $MnCoGe_{1-x}P_x$ [44], $MnCoGe_{1-x}Sn_x$ [45], $MnCo_{1-x}Cd_xGe$ [46], $MnCo_{1-x}Ti_xGe$ [47], and $Mn_{1-x}Ag_xCoGe$ [48], and iii) applying external hydrostatic pressure, for example on the alloys $Mn_{1-x}Cr_xCoGe$ [40,49], $MnCoGe_{1-x}Si_x$ [8,50-51], $MnCoGe_{1-x}Al_x$ [52], and $Mn_{1-x}Al_xCoGe$ [23]. Magneto-structural coupling has been also achieved by Cr-, B- and Cu-doping, leading to a giant magnetocaloric effect, making this alloy a promising candidate for magnetic refrigeration [39-40,53]. However, all these observations were performed in bulk materials. Recently, the composition effects [54] and alloying effects [55] on the structural and magnetic properties of intermetallic Mn-Co-Ge alloys were investigated experimentally in thin films. Furthermore, a first attempt at MnCoGe thin film production was reported using non-diffusive reaction [31]. This study showed that in these conditions, the MnCoGe compound grows from T ~ 588 K, forming a polycrystalline layer exhibiting only the hexagonal structure, which was found to be stable from 873 K to RT. The orthorhombic structure was never observed in this type of thin films, which were shown to exhibit high quality magnetic properties matching that of bulk MnCoGe in the hexagonal structure, with T_c ~ 269 K and with a negligible coercive field at RT. However, the elaboration method led to the formation of Mn-O nano-clusters (< 3 nm) periodically distributed along the film thickness, leading to an off-stoichiometry close to $Mn_5Co_6Ge_6$.

In the present study, the use of thin film RD is investigated, with the aim of forming stoichiometric MnCoGe thin films free of nano-clusters and with the orthorhombic structure that possesses a higher T_c. MnCoGe growth from a thin-film Co/Ge/Mn stack was investigated during a ramp annealing using in-situ X-ray diffraction (XRD). The structural properties of the MnCoGe films were characterized by atomic force microscopy (AFM) and transmission electron microscopy (TEM). Their composition was determined by energy dispersive X-ray spectrometry (EDS), and their magnetic properties were studied using a superconducting quantum interference device (SQUID) and ferromagnetic resonance (FMR) measurements. RD leads to the sequential formation of the binary phases at the two Co/Ge and Ge/Mn interfaces before the formation of the ternary MnCoGe phase.

2. Experiments

Four different types of samples were prepared, allowing reaction in the three binary systems Mn/Ge, Co/Ge, and Mn/Co, as well as in the ternary system Co/Ge/Mn, to be investigated. The Co, Ge, and Mn layers were deposited sequentially by magnetron sputtering in a commercial setup exhibiting a base pressure of ~ 10^{-8} Torr, allowing simultaneous sputtering of three different targets during sample rotation (5 rpm here) for thickness homogeneity. All the layers were deposited at RT in the same conditions using a 99.9999% pure Ar gas flow to sputter a 99.99% pure Mn target, a 99.999% pure Ge target and a 99.99% pure Co target. The layers were deposited on the Si native oxide of a Si(100) substrate. This SiO_2 layer was used as a diffusion barrier between the deposited layers and the Si substrate. The thickness of the layers was measured by X-ray reflectivity, and the sample surface topography was studied by AFM in air using an NT-MDT SMENA microscope in non-contact mode. For the Mn/Ge binary system, a 200 ± 10 nm-thick amorphous Ge layer was deposited on the SiO_2 layer before being covered by

a 30 ± 2 nm-thick polycrystalline Mn layer. For the Co/Ge system, a 33 ± 3 nm-thick polycrystalline Co layer was deposited on top of the same amorphous Ge layer. For the Mn/Co system, a 200 ± 6 nm-thick polycrystalline Co layer was deposited on SiO_2 and covered by a 30 ± 2 nm-thick polycrystalline Mn layer. Finally, for the ternary system, the thicknesses of the Mn, Co, and Ge layers were chosen considering the atomic densities of the three elements to match the stoichiometry of the MnCoGe compound. A 50 ± 3 nm-thick polycrystalline Mn layer was deposited on SiO_2 and capped with a 100 ± 11 nm-thick amorphous Ge layer, before the deposition of a 49 ± 2 nm-thick polycrystalline Co layer on Ge (Co/Ge/Mn system). This approach was chosen for the ternary system in order to promote reaction between the elements, since the binary systems Mn-Ge and Co-Ge form several compounds, but the phase diagram of Co-Mn corresponds to phase separation [56]. Solid-state reactive diffusion in the four different types of samples was investigated by XRD during *in situ* annealing under vacuum (~ 7×10^{-6} Torr) between 323 and 673 K in an Anton Paar TTK 450 chamber. XRD measurements were performed in the Bragg-Brentano geometry (θ–2θ) using a Cu K_α source ($\lambda_{K\alpha}$ = 1.54 Å), in an PANalytical X'Pert PRO setup equipped with an X'Celerator detector designed for high-speed data collection. For each sample, the temperature was raised from RT to 323 K, before performing the measurements up to 673 K during a heating ramp of 5 K per minute steps separated by 4 min-long XRD measurements at constant temperature, corresponding to an average heating ramp of 1 K min^{-1}. The diffractograms did not change during the temperature increase from RT to 323 K. For the ternary system, after reaching 673 K, the temperature was maintained constant for 3 days, carrying out the same 4 min-long XRD measurements separated by 20 min. Phase identification was performed using the X'Pert HighScore software package for diffraction data analysis. After annealing, the sample structure was studied by TEM in cross-

section samples prepared by focused ion beam (FIB) milling in an FEI dual beam HELIOS 600 nanolab setup. HAADF-STEM and HREM images were performed using a field emission gun (FEG) FEI Titan Cs-corrected microscope operated at 200 kV. Bright Field (BF) images, Scanning Annular Dark Field (STEM-ADF) images and EDS analyses were acquired using a LaB_6 FEI Tecnai transmission electron microscope at 200 kV. Theoretical electron diffraction (ED) patterns were calculated with the simulation software package JEMS [57] using the two-beam theory [58]. EDS analyses (line profiles) were performed using a silicon drift detector OXFORD X-max80 using a probe size of approximately 5 nm. The specimen was tilted towards the detector by an offset of 20° to ensure that all the collected X-rays corresponded to all-and-only X-rays from the region of interest, ensuring EDS quantitative measurements. The magnetic properties of the MnCoGe film were investigated using a SQUID magnetometer MPMS-XL operating in a temperature range between 1.8 and 400 K in a magnetic field up to 7 T, and using a conventional X-band Bruker EMX spectrometer (f = 9.39 GHz, T = 250 K). The FMR spectra were measured with an applied magnetic field rotated out-of-plane, and then fitted with a Lorentzian profile to extract the resonance field.

3. Results and discussion

In-situ XRD study of solid-state thin film reactive diffusion in a ternary system may be complex due to the significant number of different phases that can form and the possible overlap between the diffraction peaks of these phases. In the following, we present the in-situ XRD study of the phase formation sequence for the binary Mn/Co, Mn/Ge, and Co/Ge systems (section 3.1) before presenting a similar study in the case of the ternary Co/Ge/Mn system (section 3.2). The goal of these in-situ observations is to determine the different steps that lead to the formation of the desired film during annealing, allowing the design of a specific thermal process if necessary.

Next, we present in the two following parts the structural and chemical characterizations of the obtained MnCoGe film (section 3.3), as well as its magnetic properties (section 3.4). These characterizations allow a better understanding of the phase formation sequence, as well as clarifying on the benefits and the drawbacks of the reactive diffusion method for MnCoGe thin-film production.

3.1. Phase formation sequence in the binary Mn/Co, Mn/Ge, and Co/Ge systems

In order to facilitate the XRD study of reactive diffusion in the ternary system (sample Co/Ge/Mn), allowing the fabrication of MnCoGe thin films, thin-film solid-state reaction was first investigated in the case of the three binary systems Mn/Co, Mn/Ge, and Co/Ge. Fig. 1 shows the diffractograms recorded during XRD *in situ* annealing of the samples Mn/Co, Mn/Ge, and Co/Ge. The diffraction intensity is plotted in planar view as a function of the Bragg-Brentano angle 2θ and temperature (T). As expected, the Mn/Co diffractograms (Fig. 1a) show no reaction between Mn and Co, since no Co-Mn compounds can be formed according to the Co-Mn phase diagram [56]. Three diffraction peaks are detected after deposition: Mn(330) at $2\theta = 42.79°$, and two peaks corresponding to Co: a peak at $2\theta = 41.91°$ and the peak Co(111) at $2\theta = 44.57°$. During annealing, the intensity of the Mn peak decreases until completely disappears at the end of the experiment. Conversely, the Co peaks remain, but their positions shift towards the lower angles, which is the signature of an increased distance between the detected atomic planes. In addition, the intensity of the peak Co(111) increases with temperature from $T = 505$ K, indicating Co grain growth. These observations are in agreement with the entire dissolution of the 30-nm thick Mn film in the 200 nm-thick Co substrate. The Mn solubility limit in αCo (face centered cubic–fcc structure) in our temperature range is ~ 45 at% [56]. In our case, the entire dissolution

of Mn in Co should lead to an average Mn concentration in the Co layer of ~ 13 at%, which is significantly lower than the Mn solubility in Co. The shift of the peak Co(111) is $\Delta 2\theta = 44.38 - 44.57 = -0.19°$, which corresponds to $\Delta d_{111} = +8.25 \times 10^{-4}$ nm. Considering the αCo lattice parameter $a_{Co} = 0.35170$ nm measured in the Co film before annealing and the lattice parameter $a_{Mn} = 0.368$ nm of fcc-γMn calculated ab initio [59] according to the Vegard law [60], the shift of the Co(111) peak should correspond to that of a Co crystal containing ~ 9 at% of Mn. This value is lower than the expected 13 Mn at%, but is close enough to support the total dissolution of the Mn layer in Co due to the accuracy of a_{Mn}. Fig. 1b presents the observations made on the Mn/Ge sample. Before reaction, only the Mn(330) peak is detected at $2\theta = 42.79°$, since the Ge layer is amorphous. At T ~ 513 K, this peak starts to disappear simultaneously with the appearance of eight new peaks at 2θ = 30.92°, 35.8°, 38.71°, 42.67°, 43.78°, 52.85°, 53.16° and 56.73°, corresponding to the atomic plane families (111), (002), (210), (211), (112), (310), (212), and (311) of the Mn_5Ge_3 phase, respectively. After the total disappearance of the Mn diffraction peak, three additional peaks appear at T ~ 583 K: at $2\theta = 27.46°$, 45.56°, and 53.92°, corresponding to the Ge(111), Ge(220), and Ge(311) atomic planes, respectively. They are the signature of the 200 nm-thick Ge layer crystallization. In agreement with previous experiments performed on the Mn/Ge system using samples made by e-beam evaporation [27], phase formation is found to be sequential, the Mn_5Ge_3 phase forming first, and the low-T phase $Mn_{3.4}Ge$ and Mn_7Ge_3 being absent of the sequence. However, the phase formation sequence appears to be incomplete in the present case, since the last phase in the sequence $Mn_{11}Ge_8$ is not observed. Abbes et al. [27] observed the Mn_5Ge_3 formation at T ~ 483 K, followed by the formation of $Mn_{11}Ge_8$ and Ge crystallization at T ~ 553 K, the peaks Ge(111), Ge(220), and Ge(311) overlapping respectively with the peaks $Mn_{11}Ge_8$(311), $Mn_{11}Ge_8$(421), and $Mn_{11}Ge_8$(704) (three additional peaks of

$Mn_{11}Ge_8$ were also detected). Mn Metal-Induced-Crystallization effect [61] was found to reduce the Ge crystallization temperature of ~ 290 K. In the present case, Mn_5Ge_3 and Ge crystallization were both found to form at temperatures about 30 K higher than reported in ref 27. Furthermore, Mn_5Ge_3 is found to be stable up to 673 K. These differences may be attributed to the different methods used for sample fabrication. Fig. 1c shows XRD measurements performed during Co/Ge reaction. After deposition, two Co diffraction peaks are detected, the peak Co(111) at $2\theta = 44.57$ and the peak at $2\theta = 41.91°$. The intensities of these peaks start to decrease at $T = 523$ K, with the appearance and the development of four new peaks at $2\theta = 24.63°$, 33.34°, 46.24° and 47.64°, corresponding to CoGe(110), CoGe(–401), CoGe(112) and CoGe(020), respectively. After the total disappearance of the Co peaks, four new peaks are detected at $T = 588$ K: at $2\theta = 35.62°$, 45.08°, 46.12° and 47.48°. They respectively correspond to the atomic planes (202), (220), (204), and (115) of the phase $CoGe_2$. At $T = 658$ K, three other peaks appear at $2\theta = 27.46°$, 45.56°, and 53.92°, respectively related to Ge(111), Ge(220), and Ge(311), due to Ge crystallization. Co reduces the Ge crystallization temperature of ~ 185 K, which is about 100 K less than Mn [61]. According to the Co-Ge phase diagram, five compounds should be observed in the phase formation sequence in our temperature range: Co_5Ge_2, Co_5Ge_3, CoGe, Co_5Ge_7, and $CoGe_2$. However, the phase Co_5Ge_2, which is expected to be the first, has a very low probability of formation at the beginning of the temperature ramp, as being stable for $T > 655$ K. In our case, the phase formation is sequential, but only two phases are observed: Co_5Ge_3 does not form, CoGe is detected first, the following phase Co_5Ge_7 does not form, and $CoGe_2$, the last phase of the sequence that is the Co-richest phase in the phase diagram, is detected next. This sequence is different from the sequence reported by De Keyser et al. [62] on Ge(100) and Ge(111). CoGe, Co_5Ge_7, and $CoGe_2$ were observed to appear sequentially on Ge(100), while the phase sequence

was shown to be reduced to the formation of Co_5Ge_7 followed by the formation of $CoGe_2$ on Ge(111), Co_5Ge_7 growing in epitaxy on the Ge(111) substrate. As shown by De Keyser et al., the phase sequence being dependent on the substrate crystalline structure, the differences between their observations and our results could be linked to the initial amorphous state of our Ge substrate.

3.2. Phase formation sequence in the ternary Co/Ge/Mn system

Fig. 2a presents an AFM image obtained of the Co/Ge/Mn sample after magnetron sputtering deposition. The sample surface shows a root mean squared (RMS) surface roughness less than 0.1 nm, and Co grain boundaries cannot be observed. Fig. 3 presents the variations of the X-ray diffractogram versus temperature acquired during *in situ* annealing of the Co/Ge/Mn sample, with the aim of growing an MnCoGe thin film. After deposition (Fig. 3a), two diffraction peaks are detected at $2\theta = 42.79°$ and 44.37°, corresponding to Mn(330) and Co(111). These two peaks were also initially detected in the case of the binary systems Mn/Ge and Co/Ge. At T = 510 K, the Mn peak intensity starts to decrease as three new peaks appear at $2\theta = 38.1°$, 42.2° and 43.54°, corresponding to Mn_5Ge_3(210), Mn_5Ge_3(211), and Mn_5Ge_3(112), respectively (Fig. 3a). These three peaks were also observed to appear at the same temperature in the sample Mn/Ge, but in this case, they formed along with five additional diffraction peaks related to the atomic planes (111), (002), (310), (212), and (311) of the phase Mn_5Ge_3. The diffraction peak Co(111) starts to disappear slightly latter at T = 526 K, with the simultaneous apparition of two peaks at $2\theta = 24.63°$ and 47.64°, respectively related to the atomic planes (110) and (020) of the phase CoGe (Fig. 3a). These two peaks appeared at the same temperature in the case of the binary system Co/Ge, but together with the two diffraction peaks CoGe(−401) and CoGe(112). After the

complete disappearance of the Co peak, the intensities of the two CoGe peaks start to decrease simultaneously at T = 573 K, while a new peak corresponding to $CoGe_2$(204) appears at 2θ = 46.12° (Fig. 3a). $CoGe_2$ was found to form at a slightly higher temperature (+ 15 K) in the Co/Ge sample, exhibiting three additional diffraction peaks. When the temperature of 673 K is reached, the diffractogram is identical, only the phases Mn_5Ge_3 and $CoGe_2$ are detected (Fig. 3a). Consequently, up to this stage, only the binary compounds were formed, exactly following the phase formation sequences observed in the Mn/Ge and Co/Ge samples, suggesting that the reactions observed so far were all taking place at the Mn/Ge and Co/Ge interfaces in the Co/Ge/Mn sample. However, as the Ge crystallization was not detected, it is difficult to conclude whether a layer of pure Ge is still present in the sample, corresponding to the Mn_5Ge_3/Ge/$CoGe_2$ Stack. Furthermore, it can be noted that the consumption of the entire 50 nm-thick Mn layer to form a Mn_5Ge_3 layer would also consume about 60 nm of Ge; and the consumption of the 50 nm-thick Co layer to form a $CoGe_2$ layer would need about 200 nm of Ge. Since only 100 nm of Ge is present in the sample, pure Mn and pure Co should still be present in the sample at that stage (Mn/Mn_5Ge_3/Ge/$CoGe_2$/Co stack). The fact that Mn and Co are not detected can be explained by a texture change preventing detection in our diffraction conditions θ–2θ. After 40 min at T = 673 K (Fig. 3b), the intensities of the three diffraction peaks of Mn_5Ge_3 start to decrease simultaneously with the detection of three new peaks at 2θ = 29.24°, 41.5° and 44.54°, corresponding to $Mn_{11}Ge_8$(402), $Mn_{11}Ge_8$(601), and $Mn_{11}Ge_8$(323) respectively. This suggests that some pure Ge is still available in the sample, since $Mn_{11}Ge_8$ grows without consuming $CoGe_2$ (Mn/Mn_5Ge_3/$Mn_{11}Ge_8$/Ge/$CoGe_2$/Co stack). After 60 min at T = 673 K, Mn_5Ge_3 is no longer detectable and the intensities of the diffraction peaks of $CoGe_2$ start to decrease, with the appearance and growth of four new peaks at 2θ = 30.2°, 42.04°, 44.2° and 56.24°, which

respectively correspond to the atomic planes (101), (102), (110) and (112) of Hexa-MnCoGe (Fig. 3b). The growth of Hexa-MnCoGe does not consume $Mn_{11}Ge_8$, suggesting that Hexa-MnCoGe grows by consuming $CoGe_2$ and the unreacted Mn and Co reserves ($Mn_{11}Ge_8$/Mn/Hexa-MnCoGe/$CoGe_2$/Co stack). 20 min later, the diffraction peaks of $Mn_{11}Ge_8$ start to decrease simultaneously with the appearance of a new diffraction peak at $2\theta = 45.34°$, corresponding to the plane (402) of Mn_5Ge_2, concurrently with the consumption of $CoGe_2$ and the growth of Hexa-MnCoGe (Fig. 3b). This suggests that the Mn reserve has been consumed. Hexa-MnCoGe reached $Mn_{11}Ge_8$ ($Mn_{11}Ge_8$/Hexa-MnCoGe/$CoGe_2$/Co stack), and started to consume it, lowering the Mn concentration at the interface $Mn_{11}Ge_8$/Hexa-MnCoGe, triggering the formation of Mn_5Ge_2 at this interface ($Mn_{11}Ge_8$/Mn_5Ge_2/Hexa-MnCoGe/$CoGe_2$/Co stack). Mn_5Ge_2 contains less Ge than Mn_5Ge_3 with a Ge composition close to 30% that is close to the Ge composition in the ternary phase MnCoGe. Thus, it should appear before Mn_5Ge_3 during Mn/Ge reaction assuming similar Mn and Ge self-diffusion kinetics in Mn_5Ge_2 and Mn_5Ge_3 [63]. However, Mn_5Ge_2 is stable only for $T > 893$ K [56], which explains why it has not been observed before in our annealing conditions ($T \leq 673$ K). $CoGe_2$ vanishes after 100 min at 673 K before $Mn_{11}Ge_8$ ($Mn_{11}Ge_8$/Mn_5Ge_2/Hexa-MnCoGe/Co stack). $Mn_{11}Ge_8$ vanishes when the diffraction peak related to Mn_5Ge_2 reaches its maximum intensity (Mn_5Ge_2/Hexa-MnCoGe/Co stack). After 380 min at $T = 673$ K, the Mn_5Ge_2 peak starts to disappear as four new peaks appear at $2\theta = 41.2°$, 46.86°, 47.63° and 57.8°, which respectively correspond to the planes (103), (020), (113), and (312) of Ortho-MnCoGe (Fig. 3b). This suggests that Ortho-MnCoGe forms at the Mn_5Ge_2/Hexa-MnCoGe interface. At that stage, Mn_5Ge_2 is consumed concurrently with the growth of both Hexa-MnCoGe and Ortho-MnCoGe, supporting the assumption that pure Co is still available in the sample. After 2020 min at 673 K, the intensity of the diffraction peaks of

Hexa-MnCoGe reaches a maximum and starts to decrease until the end of the experiment. 500 min later, Mn_5Ge_2 vanishes, while Ortho-MnCoGe continues to grow until the end of the annealing, consuming Hexa-MnCoGe. Fig. 4 shows the variations of the normalized intensity of selected diffraction peaks as a function of the XRD scan number. Each diffraction peak was fitted with a Gaussian law before being integrated and finally normalized to their maximum. The normalized intensity of a given diffraction peak can be considered to be proportional to the volume of the considered phase. The scans from n = 1 to 71 correspond to the temperature ramp from T = 323 to 673 K, and the scans from n = 72 to 288 correspond to the following isothermal annealing at 673 K for 3 days. For clarity, the binary phases corresponding to the reactions taking place at the Mn/Ge interface are presented in Fig 4a, while the binary phases related to the reactions at the Ge/Co interface are presented in Fig. 4b. The ternary phases are presented in the two figures. A number has been given to each diffraction peak according to its place in the phase formation sequence. Six diffraction peaks are reported in Fig. 4a: Mn(330), #1 Mn_5Ge_3(112), #4 $Mn_{11}Ge_8$(420), #5 Hexa-MnCoGe(102), #6 Mn_5Ge_2(402), and #7 Ortho-MnCoGe(113); and five diffraction peaks are reported in Fig. 4b: Co(111), #2 CoGe(020), #3 $CoGe_2$(204), #5 Hexa-MnCoGe(102), and #7 Ortho-MnCoGe(113). These figures allow the sequential growth and consumption of the phases to be more easily followed. The XRD observations correspond to complex atomic redistributions, most likely not related to reactions at flat interfaces. Abbes et al. [27] showed in their experiments that the interface between Mn_5Ge_3 and polycrystalline Ge (poly-Ge) was not flat, and that $Mn_{11}Ge_8$ was growing between Mn_5Ge_3 and poly-Ge, forming faceted “fingers” extending through the Mn_5Ge_3 layer (up to the surface) and the poly-Ge layer. Such significant interfacial roughness, probably due to grain boundary (GB) growth, may lead to complex bulk reactions. At the end of the experiment, only the ternary compound MnCoGe is detected with a majority proportion exhibiting the hexagonal structure, and a minority proportion

exhibiting the orthorhombic structure. Due to the formation of Ortho-MnCoGe after the appearance and the growth of Hexa-MnCoGe, and due to the constant growth of Ortho-MnCoGe in parallel with the constant consumption of Hexa-MnCoGe at the end of the isothermal annealing at 673 K, the film is expected to have exhibited the orthorhombic structure if the annealing would have been maintained as long as necessary. However, as shown in Fig. 5, the intensities of the diffraction peaks of Ortho- and Hexa-MnCoGe do not change when the sample is cooled from 673 K to RT, meaning that the hexagonal/orthorhombic transition is nevertheless not observed in the film. This is unusual, since Ortho-MnCoGe should be stable at low temperatures (T < 420 K for stoichiometric MnCoGe). However, ab initio calculations showed that a decrease of Mn concentration in the MnCoGe compound (off-stoichiometric MnCoGe compound) leads to a decrease of the energy difference between Hexa- and Ortho-MnCoGe [64], and experiments showed that, in this case, the transition temperature T_t can be lower than RT [65]. Thus, the stabilization of Hexa-MnCoGe can be explained by a lack of Mn in the MnCoGe compound. Nevertheless, in this case, it seems difficult to explain the growth of Ortho-MnCoGe at high temperature in our experiments. Indeed, assuming that these X-ray diffractogram variations are not linked to a texture effect, this phenomenon could be understood if the structural transition was kinetically limited and the transition temperature T_t was higher than 673 K in our case. According to the calculations [64], the hydrostatic expansion of the lattice unit cells (isotropic tensile stress) of Ortho- and Hexa-MnCoGe should promote the formation of the orthorhombic structure. Thus, tensile stress could also explain the stabilization of Ortho-MnCoGe at high temperature in our films. When the Hexa-MnCoGe phase is first detected, the four detected diffraction peaks (101), (102), (110), and (112) are found to be shifted towards smaller 2θ angles, which correspond to larger distances d_{hkl} between interatomic planes (h,k,l).

Considering that $d_{hkl} = [4(h^2+hk+k^2)/3a^2 + (l/c)^2]^{-1/2}$ with a, b, and c the lattice parameters of the hexagonal structure, and h, k, and l the Miller indices [66], the measured angles 2θ = 30.2°, 42.04°, 44.2°, and 56.24° give $a = b$ = 0.409 nm and c = 0.540 nm with an error of ± 0.5%. The lattice parameters of as-detected Hexa-MnCoGe are larger than usual, since the standard lattice parameters of stoichiometric Hexa-MnCoGe at RT are $a = b$ = 0.4080 nm and c = 0.5303 nm [67]. Then, the four Hexa-MnCoGe diffraction peaks shift back to higher angles during Hexa-MnCoGe growth, towards the regular Hexa-MnCoGe parameters, in agreement with the effect of a (mechanical or chemical) relaxation mechanism. The relaxation stops after 240 min at 673 K, the diffraction peaks (101), (102), (110), and (112) being respectively detected at 2θ = 30.32°, 42.28°, 44.32° and 56.52°, corresponding to $a = b$ = 0.408 nm and c = 0.536 nm. Similar results are obtained at the end of the experiment at RT (Fig. 5), the same diffraction peaks being detected at 2θ = 30.33°, 42.31°, 44.32°, and 56.52°, corresponding to $a = b$ = 0.408 nm and c = 0.535 nm. Considering experimental error, the Hexa-MnCoGe phase appears to be relaxed at RT. The volume difference experienced by the Hexa-MnCoGe phase at T = 673 K, between the beginning and the end of its growth is ~ −1.1 %, its volume variation at the end of the experiment due to sample cooling from 673 K to RT being ~ −0.15 %. Ab initio calculations [64] showed that an increase of the parameters $a = b$ and c can be the signature of a decreased Mn concentration in the MnCoGe compound in the paramagnetic state ($T > T_c$). According to these calculations, a lack of Mn should also lead to a reduced T_c. The shift of the Hexa-MnCoGe diffraction peaks observed in our experiments could be due to either the relaxation of tensile stress built in the film at the beginning of its formation, due to volume differences between the phases in the sample ($Mn_{11}Ge_8$, $CoGe_2$, and Hexa-MnCoGe) for example [68], or due to the formation of an off-stoichiometric Hexa-MnCoGe compound lacking Mn at the growth beginning, getting richer in

Mn during the growth. It can be noted that the end of the relaxation, occurring after 240 min at 673 K, does not correspond to the formation or the disappearance of any of the detected phases.

3.3. Structural and chemical analyses of the MnCoGe film

Fig. 2b presents AFM measurements performed on the MnCoGe film surface after XRD *in situ* annealing. The MnCoGe surface is rougher after reaction, showing a surface RMS of ~ 4.0 ± 0.5 nm. MnCoGe grains are apparent, exhibiting an average lateral size of ~ 84 ± 5 nm. The MnCoGe film obtained after XRD in situ annealing was also characterized by TEM. Fig. 6 shows BF images giving a global picture of the cross-sectional sample. The thickness of the MnCoGe layer is ~ 150 nm as expected, considering the atomic density and the thickness of the initial Co, Ge, and Mn films. The TEM images clearly show that, contrasting with non-diffusive reaction (NDR) [31], MnCoGe growth by RD promoted the formation of pores in the film, exhibiting sizes comprised between few nanometers to about 30 nm. The presence of pores in the film can be explained by the differences between the diffusion coefficients (direct vacancy mechanism) of the three elements Mn, Co, and Ge in the different growing phases during RD (Kirkendall porosity) [69]. The pores are distributed either along horizontal planes, as expected for vacancy accumulation at interfaces during interfacial reaction, or along lines perpendicular to the surface, which is more likely linked to reaction at GBs, suggesting complex MnCoGe growth with both 2D (interfacial reaction) and 3D (GB reaction) growth. Fig 6a also shows two unexpected layers located beneath the native SiO_2 layer initially separating the Si substrate from the deposited film: a 5 nm-thick continuous layer with a bright contrast, and a discontinuous 20 nm-thick layer with a darker contrast. The discontinuity of the latter is shown in Fig 6b and Fig 6c, with a discontinuity point located in the middle of the TEM image (arrow) in Fig 6b, and a region of the sample without this layer underneath in Fig 6c. In order to identify the crystalline structures of

the MnCoGe film, several power spectra were recorded from HREM images of grains and then compared with simulated patterns. Fig 7 presents 3 different cross-sectional bright field images taken at three different locations in the film. These three images are representative of the phase distribution observed in the sample. Three different phases are detected in the film after in situ annealing: the Hexa-MnCoGe phase, the Ortho-MnCoGe phase, and the monoclinic CoGe phase (mono-CoGe). The two MnCoGe phases are well detected by XRD, Hexa-MnCoGe being consumed by Ortho-MnCoGe before annealing is stopped. However, CoGe is not observed in the XR diffractograms. Due to the size and density of CoGe grains observed in TEM images, the lack of CoGe diffraction peaks in diffractograms is probably due to the CoGe grain texture compared to the Bragg-Brentano diffraction geometry. Hexa-MnCoGe is found to form large grains extending through the entire layer (columnar grains) as shown in Fig. 7a, or grains that start from the bottom of the layer (Mn-rich region) but stop before reaching the surface, as they are in contact with either an Ortho-MnCoGe grain (Fig. 7b) or a mono-CoGe grain (Fig. 7c) located at the surface. The power spectra (Fig. 7d) recorded from the HREM image of the Hexa-MnCoGe grain shown in Fig. 7a (white contour) is in agreement with the $[423]_h$ zone axis of the hexagonal ternary MnCoGe crystal phase (Fig. 7g) [70]. The calculated distances from the literature structure files $q_{(-120)h}$ = 2.08 Å and $q_{(21-2)h}$ = 1.64 Å are in agreement with the measured distances with an error less than 0.1 Å. As previously pointed out, this result also suggests that the Hexa-MnCoGe phase grown by RD is relaxed and stoichiometric. Fig. 7b presents a grain (white contour) identified as the orthorhombic ternary MnCoGe crystal phase [70]. It exhibits a lateral size of ~ 150 nm (direction parallel to the surface) and a thickness of ~ 50 nm (direction perpendicular to the surface). The fact that Ortho-MnCoGe grains show smaller sizes and densities than Hexa-MnCoGe grains suggests that the Ortho-MnCoGe phase grew for a shorter period of time during annealing. This is in agreement with in situ XRD measurements, showing

that Ortho-MnCoGe formes after the growth of the Hexa-MnCoGe phase. The distance and the position of the reflections $q_{(2\text{-}1\text{-}1)o}$ = 2.28 Å and $q_{(23\text{-}3)o}$ = 2.02 Å (Fig. 7e and 7h) are in agreement with the $[324]_o$ zone axis of the attributed system, suggesting that the Ortho-MnCoGe phase grown by RD is also relaxed and stoichiometric. As previously mentioned, the Ortho-MnCoGe grain is located at the surface of the sample, which corresponds to the Co-rich region. Fig. 7c shows a mono-CoGe grain (white contour) also located at the surface of the layer, in the Co-rich region. The distance and the position of the reflections $q_{(20\text{-}1)m}$ = 4.11 Å and $q_{(\text{-}42\text{-}2)m}$ = 1.14 Å are in agreement with the $[142]_m$ zone axis of the given system (Fig. 7f and 7i). In order to unambiguously confirm the identification of the monoclinic binary structure, we have compared the measured plane distances to the ternary orthorhombic and hexagonal distances. Concerning $q_{(20\text{-}1)m}$ = 4.11 Å , the closest planes belonging to the Hexa-MnCoGe ternary system are $q_{(001)h}$ = 5.27 Å and $q_{(100)h}$ = 3.55 Å, that give respective difference values of $\Delta q_{(001)h}$ = 1.16 Å and $\Delta q_{(100)h}$ = 0.56Å. The closest planes belonging to the Ortho-MnCoGe ternary system are $q_{(101)o}$ = 4.52 Å and $q_{(010)o}$ = 3.8 Å, that also give respective difference values equal to $\Delta q_{(001)h}$ = 0.41 Å and $\Delta q_{(100)h}$ = 0.31 Å.

Fig. 8a presents an ADF-STEM image of the same layer formed after RD of the Co/Ge/Mn stack. EDS measurements showed that the large grain with a bright contrast in the center of the ADF-STEM image corresponds to MnCoGe. Fig. 8b presents two EDS profile lines performed in STEM mode on the same cross-sectional sample as shown in Fig. 8a, along two different line-scans displayed as white arrows in Fig. 8a (line 1 and line 2). The compositions measured by EDS result from the signal summation over the entire sample thickness. The signal of five elements was examined: Si, O, Ge, Co, and Mn. The composition along the line 1 shows three regions: i) close to the surface the EDS signal shows a region (white contour in Fig. 8a) corresponding to the overlap (in the thickness) between MnCoGe and CoGe grains, ii) in the

center of the sample the composition corresponds to stoichiometric MnCoGe (in the measurement error range ~ 2%), and iii) between the film and the Si substrate, the continuous 5 nm-thick bright layer observed in Fig. 6 is identified as an Mn oxide layer (Mn_xO_y). This layer probably results from the reaction of Mn with the thin native SiO_2 layer (~ 2 nm) on which Mn was initially deposited. The line 2 shows similar composition variations, exhibiting a larger region containing CoGe grains and a smaller region corresponding only to MnCoGe, but also allows the discontinuous 20 nm-thick layer located underneath the film (Fig. 6) to be identified as an Mn silicide (Mn_xSi_y). The distribution of Co, Si, Ge, and Mn atoms in the sample was confirmed by 2D chemical maps (Fig. 8c). TEM observations show the systematic presence of CoGe grains in the Co-rich region close to the surface if an Mn_xSi_y layer is located in the Mn-rich region close to the Si substrate. Columnar Hexa-MnCoGe grains are observed only in regions free of Mn_xSi_y layers. These observations suggest that the Mn reaction with the SiO_2 layer during annealing led to local Mn leakage into the Si substrate, promoting the local formation of Mn silicide below the Mn-Co-Ge film. The consumption of part of the deposited Mn film to form Mn_xO_y and Mn_xSi_y layers suggests that an existing Mn reservoir as formerly proposed to interpret in situ XRD is not realistic (Mn/Mn_5Ge_3/Ge/$CoGe_2$/Co stack). Instead, due to the reduced amount of Ge, it seems more reasonable that the Ge layer was fully consumed at both interfaces Mn/Ge and Co/Ge before the formation of the ternary phase, allowing the Mn_5Ge_3/$Mn_{11}Ge_8$/$CoGe_2$/CoGe stack to be formed, the disappearance of the diffraction peaks of Mn_5Ge_3 and CoGe being partly due to a texture change of these two layers. In the case of polycrystalline layers, previous TEM observations [27] showed that the $Mn_{11}Ge_8$ layer interfaces are significantly rough due to $Mn_{11}Ge_8$ growth in GBs, part of the Mn_5Ge_3 layer being surrounded by the $Mn_{11}Ge_8$ phase. In this case, Hexa-MnCoGe could grow along GBs at the beginning, consuming $CoGe_2$ and Mn_5Ge_3, the latter not being detected by XRD due its texture,

incompatible with the Bragg-Brentano diffraction geometry. As mentioned before, the 3D growth of the ternary phase is supported by the pores observed along GBs. Later on, $Mn_{11}Ge_8$ starts to be also consumed by the Hexa-MnCoGe growth, leading to Mn_5Ge_2 formation. This phase is not stable at the considered temperature, but contains less Mn than $Mn_{11}Ge_8$ and possesses a Ge concentration similar to the ternary compound. Thus, the phases present in the sample should form the $Mn_{11}Ge_8$/Mn_5Ge_2/Hexa-MnCoGe/$CoGe_2$/CoGe stack at that stage. From there, Hexa-MnCoGe could grow by consuming all the other phases. However, due to the inhomogeneous consumption of Mn to form the Mn_xSi_y layer underneath the Mn-Co-Ge layer, Hexa-MnCoGe growth is not homogeneous. Hexa-MnCoGe can grow in the entire film thickness forming columnar grains in regions free of Mn silicide (Fig. 7a). However, in regions where Mn_xSi_y has formed, Hexa-MnCoGe grows toward the Mn-rich region consuming the entire $CoGe_2$ layer, but leaving part of the CoGe layer close to the surface, depending on the local Mn shortage induced by Mn_xO_y and Mn_xSi_y growth (Fig. 7c). In some regions where Hexa-MnCoGe has reached the sample surface, the Ortho-MnCoGe phase nucleates close to the surface and grows into the layer consuming Hexa-MnCoGe towards the substrate (Fig. 7b). Due to the variation of the Mn amount in the Mn-rich region close to the Si substrate, depending on the location in the sample, Hexa-MnCoGe growth consuming Mn_5Ge_2 and $CoGe_2$ can occur simultaneously with the growth of Ortho-MnCoGe consuming Hexa-MnCoGe. Indeed, before Ortho-MnCoGe formation, in situ XRD shows (Fig. 4) that the rapid Hexa-MnCoGe growth occurs simultaneously with a rapid consumption of Mn_5Ge_2. Once Ortho-MnCoGe growth is detected by XRD, the Hexa-MnCoGe growth rate and the Mn_5Ge_2 consumption rate slow down simultaneously, and once Mn_5Ge_2 is entirely consumed, Ortho-MnCoGe is observed to grow with the simultaneous consumption of Hexa-MnCoGe. The entire phase formation sequence during reactive diffusion of the Co/Ge/Mn stack is summarized in Fig. 9.

Further analyses of the Mn silicide layer show that this layer is actually composed of two different silicides. Fig. 10a presents a STEM-HAADF image of the sample. The Mn_xSi_y layer is composed of two layers, the layer closer to the Mn-Co-Ge film exhibiting a brighter contrast (Fig. 10a). As the obtained intensity is proportional to the mean atomic number $Z^{1.5}$ along the projection [71], the silicide layer located close to the Mn-Co-Ge film can be considered as having a higher atomic ratio Mn(Z = 25)/Si(Z = 14) than the silicide layer located close to the Si substrate. The BF inset image (white square in Fig. 10a) highlights the existence of different chemical compositions in the two Si-Mn layers. The corresponding HREM images (Fig. 10b and 10c) display the crystalline nature of the layers that therefore should correspond to Mn_pSi_q compounds. The power spectra recorded in a square area of the silicide layer close to the substrate (Fig. 10b) shows the fundamental reflections of the Si cubic structure in [100] zone axis orientation (white circles in fig. 10b). It also contains columns that are perpendicular to $\boldsymbol{q_{004}}$ whose reflections are much closer along $\boldsymbol{q_{040}}$, describing a pattern in agreement with a Higher Manganese Silicide (HMS) crystal structure. The ED patterns were calculated for all possible tetragonal HMS structures Mn_4Si_7 [72], $Mn_{11}Si_{19}$ [73-74], $Mn_{15}Si_{26}$ [75] and $Mn_{27}Si_{47}$ [76]. The [010] zone axis (Fig. 10c) exhibits the same features as those of the experimental power spectra. In fig. 10b, the minimum distance q_1 = 12 Å measured between two strong reflections along $\boldsymbol{c^*}$ (white lines) could correspond to the (004) atomic planes of the $Mn_{11}Si_{19}$ phase (red square). Some less intense reflections can also reveal the presence of (004) planes (q_2 = 48 Å) belonging to the $Mn_{27}Si_{47}$ phase. Both phases $Mn_{11}Si_{19}$ and $Mn_{27}Si_{47}$ have the same tetragonal space group P-4n2 and the same unit cell parameter values a = b = 0.55 nm, but have a different c-axis. For example, the red triangle in fig. 10b is centered on the common (200) reflection of the two silicides $Mn_{11}Si_{19}$ and $Mn_{27}Si_{47}$. The power spectrum of the second HMS layer (brighter) shows the same reflections separated by a 12 Å-distance that can be attributed to $Mn_{11}Si_{19}$. No

additional reflection is observed inside, excluding the presence of another phase in this layer, in accordance with the calculated ED. Thus, it can be concluded that two HMS phases are present in the Mn_xSi_y layer: the $Mn_{11}Si_{19}$ phase with the atomic ratio Mn/Si = 0.579, and the $Mn_{27}Si_{47}$ phase with the smaller atomic ratio Mn/Si = 0.574, the Si-richer phase being located close to Si as expected.

Contrasting with NDR [31], RD promotes the growth of MnCoGe films exhibiting properties closer to bulk MnCoGe at thermodynamic equilibrium: i) no Mn_xO_y nano-clusters, ii) stoichiometric composition, and iii) presence of the orthorhombic structure at RT. However, RD needs a significantly higher thermal budget than NDR in order to form the MnCoGe film. Furthermore, the different melting temperatures (and cohesive energies) between the three elements Co (1768 K), Mn (1519 K), and Ge (1211 K) leads to significant differences between self-diffusion coefficients in the considered phases, promoting diffusion asymmetries [69,77], and thus promoting the formation of pores in the film. Concerning thermodynamic equilibrium, in the case of stoichiometric bulk MnCoGe, the phase transition Ortho-MnCoGe/Hexa-MnCoGe occurs at T_t ~ 420 K [7-8,23,39-41]. In the present case, Hexa-MnCoGe forms first at T = 675 K in agreement with thermodynamic. However, Ortho-MnCoGe is unexpectedly observed to grow at that same temperature ($T >> T_t$) at the expense of Hexa-MnCoGe. Furthermore, Hexa-MnCoGe does not transform into Ortho-MnCoGe at RT ($T < T_t$). The stability of Hexa-MnCoGe at RT in MnCoGe films produced by NDR was previously attributed to stoichiometry variations (decrease of Mn concentration) in the MnCoGe layer linked to the formation of Mn_xO_y nano-clusters, decreasing the phase transition temperature T_t [31]. In the present case, Hexa- and Ortho-MnCoGe grains are found to be relaxed and stoichiometric. However, Ortho-MnCoGe grains being located at the surface of the MnCoGe film, surface energy minimization could be

involved in the growth/stability competition observed between Hexa- and Ortho-MnCoGe in the film geometry.

3.4. Magnetic properties of the MnCoGe film

Fig. 11 presents SQUID measurements performed on the MnCoGe film using a magnetic field applied in the plane of the sample. The diamagnetic contribution from the Si substrate was subtracted, leaving only the ferromagnetic signal from the film. Fig. 11a presents the sample magnetization (M), normalized by the measured phase volume (A m^{-1}) versus temperature in the plane of the film under an in-plane magnetic field (H) of 1 T. M is found to be about 7 % smaller than that measured on bulk Hexa-MnCoGe [78]. As expected, M decreases when T increases, since M should tend to zero toward the Curie temperature of the material. However, two decreasing slopes are observed: a first slope (red dash line in Fig. 11a) corresponding to the decrease of ~ 92 % of the magnetization, suggesting a Curie temperature lower than 300 K, and a second slope between 300 and 400 K, corresponding to the extinction of the last part of M (~ 8 %) for T close to 350 K. In order to precisely determine the Curie temperature of the film, the dynamic response of the magnetization of the sample was recorded as a function of temperature at field $H = H_0 \sin(2\pi ft)$ with $H_0 = 3 \times 10^{-4}$ T and $f = 100$ Hz, allowing the ferromagnetic/paramagnetic transition to be determined from the variation of the AC susceptibility $\chi(f) = \chi'(f) + i\chi''(f)$ in this case. Fig. 11b shows the real (χ') and imaginary (χ'') susceptibilities as a function of temperature, measured respectively in-phase and out-of-phase at a frequency $f = 100$ Hz with an applied AC field $H_0 = 3 \times 10^{-4}$ T. The Curie temperature of the MnCoGe film is found to be close to 269 K, which corresponds to the T_c of Hexa-MnCoGe [9-13,33]. XRD (Fig. 5) and TEM measurements show that the volume fraction of Ortho-MnCoGe

is significantly smaller than the volume fraction of Hexa-MnCoGe in the film. Therefore, zero-field cooling (ZFC) and field cooling (FC) magnetization measurements as a function of temperature were also carried out in-plane of the film under a small magnetic field of 1×10^{-2} T, aiming to reduce the paramagnetic signal belonging to the hexagonal phase (T_c = 269 K) between T = 300 and 380 K. This temperature range was chosen because the usual ferromagnetic/paramagnetic transition of Ortho-MnCoGe occurs at T_c ~ 355 K [23,42,79-81]. As shown in Fig. 11c, the magnetization vanishes near T = 353 K, indicating the presence in the sample of a second ferromagnetic phase with T_c = 353 K corresponding to Ortho-MnCoGe. Fig. 11d presents magnetic hystereses measured at T = 2 and 250 K. The hystereses are narrow with $H_c = 3.6 \times 10^{-2}$ T and 4×10^{-3} T at T = 2 and 250 K, respectively, which can be important for magnetocaloric applications for example, avoiding magnetic-work losses due to the rotation of the magnetic domains in a magnetic-refrigeration cycle.

FMR spectra were measured on the MnCoGe thin film under in-plane ($\varphi_H = 0°$) and out-of-plane ($\varphi_H = 90°$) magnetic field. The spectra were adjusted to a Lorentzian profile in order to extract the resonance fields. Typical spectra measured at T = 250 K are shown in Fig. 12a. The sample shows a small FMR linewidth which is directly related to the magnetic and the structural quality of the material [30,82-83]. The angular variation of the resonance field H_{res} is shown in Fig. 12b at T = 250 K. For polycrystalline film, all directions in the plane of the film are equivalent. Therefore, the magnetic field is chosen to be rotated out of the plane. The $H_{res}(\varphi_H)$ curve indicates an in-plane easy axis with a minimum resonance field of 2.67×10^{-1} T for φ_H = 0°. The hard axis is perpendicular to the plane of the film and has the highest H_{res} of 4.87×10^{-1} T. The experimental FMR data of the out-of-plane dependence of the resonance field can be well simulated using the Chappert model [84] (solid red line in Fig. 12b), and the anisotropy fields can

be extracted. The anisotropy constants can be found by using the sample magnetization determined from the static magnetic measurements. The value of the magnetization density at T = 250 K taken from Fig. 11a is $M_s = 121 \times 10^3$ A m^{-1} and the measured gyromagnetic ratio $\lambda/2\pi$ = 28 GHz T^{-1}. The resulting anisotropy constants are found to be $K_1 = 6.92 \times 10^2$ J m^{-3} and $K_2 = -1.61 \times 10^3$ J m^{-3} at T = 250 K. From the positive sign of K_1 and $K_2 > -K_1$, and according to the shape of the curve $H_{res}(\varphi_H)$ with $(H_{res})_\perp > (H_{res})_{//}$, it can be deduced that the preferential magnetization direction in the film is in the film plane, as expected due to the large shape contribution that dominates from the film geometry.

SQUID and FMR measurements are in agreement with TEM and XRD measurements, suggesting that RD promoted the formation of a stoichiometric and relaxed polycrystalline MnCoGe film containing both the orthorhombic and hexagonal structures, the latter being in a significantly larger proportion.

4. Conclusion

In summary, polycrystalline MnCoGe thin films were grown by reactive diffusion up to 400 °C between three stacked Co, Ge, and Mn nano-layers deposited on the native SiO_2 layer of a Si(001) substrate using magnetron sputtering. XRD, TEM, SQUID, and FMR characterizations show the presence of both hexagonal and orthorhombic structures, in their stoichiometric and relaxed states. However, due to the formation of Mn oxide and Mn silicides at the interface with the SiO_2/Si(001) substrate, grains of the binary CoGe phase are also present in the film.

Reactive diffusion of the ternary stack is shown to follow first the phase formation sequences of the binary systems Mn/Ge and Co/Ge, before the formation of a single ternary phase: the stoichiometric MnCoGe phase. Reactive diffusion promotes the fabrication of

MnCoGe thin films exhibiting properties closer to bulk MnCoGe compared to non-diffusive reaction. However, this method necessitates higher thermal budget and can lead to greater inhomogeneity in the film. Reactive diffusion leads to the formation of pores in the film with sizes up to 30 nm due to self-diffusion asymmetries between the diffusing species, and promotes the co-existence of the MnCoGe orthorhombic and hexagonal structures. Furthermore, the thermal treatment led to the deterioration of the SiO_2 layer by allowing SiO_2 to react with Mn, leading to Mn reactive diffusion with Si, decreasing the Mn amount in the Mn-Co-Ge film. Despite the lack of Mn, and in contrast with non-diffusive reaction, MnCoGe was grown with the correct stoichiometry but leaving CoGe grains in the film. Despite the structural (nano-pores, Hexa- and Ortho-MnCoGe) and chemical (CoGe and MnCoGe) inhomogeneities, the Mn-Co-Ge film shows good magnetic properties, with narrow FMR lines.

Acknowledgement

This work was supported by the French government through the program "Investissements d'Avenir A*MIDEX" (Project APODISE, no. ANR-11-IDEX-0001-02) managed by the National Agency for Research (ANR). R. C. thanks the University of Bordeaux, the CNRS and the "Nouvelle Région Aquitaine".

REFERENCES

[1] I. Žutić, J. Fabian, S. Das Sarma, Spintronics: Fundamentals and applications, Rev. Mod. Phys. 76 (2004) 323.

[2] C. Chappert, A. Fert, F. Nguyen Van Dau, The emergence of spin electronics in data storage, Nature Mat. 6 (2007) 813.

[3] T. Schäpers, Semiconductor Spintronics, Walter de Gruyter GmbH, Berlin/Boston, 2016.

[4] K. Uchida, S. Takahashi, K. Harii, J. Ieda, W. Koshibae, K. Ando, S. Maekawa, E. Saitoh, Observation of the spin Seebeck effect, Nature 455 (2008) 778.

[5] M. Johnson, Spin caloritronics and the thermomagnetoelectric system, Solid State Communications 150 (2010) 543.

[6] S. Bosu, Y. Sakuraba, K. Uchida, K. Saito, T. Ota, E. Saitoh, K. Takanashi, Spin Seebeck effect in thin films of the Heusler compound Co_2MnSi, Phys. Rev. B 83 (2011) 224401.

[7] E.K. Liu, H.G. Zhang, G.Z. Xu, X.M. Zhang, R.S. Ma, W.H. Wang, J.L. Chen, H.W. Zhang, G.H. Wu, L. Feng, X.X. Zhang, Giant magnetocaloric effect in isostructural MnNiGe-CoNiGe system by establishing a Curie-temperature window, Appl. Phys. Lett. 102 (2013) 122405.

[8] J.W. Lai, Z.G. Zheng, R. Montemayor, X.C. Zhong, Z.W. Liu, D.C.Zeng, Magnetic phase transitions and magnetocaloric effect of $MnCoGe_{1-x}Si_x$, J. Magnetism and Magnetic Mat. 372 (2014) 86.

[9] S. Gardelis, C.G. Smith, C.H.W. Barnes, E.H. Linfield, D.A. Ritchie, Spin-valve effects in a semiconductor field-effect transistor: A spintronic device, Phys. Rev. B 60 (1999) 7764.

[10] A. Aharony, O. Entin-Wohlman, Y. Tokura, S. Katsumoto, Spin filtering by a periodic spintronic device, Phys. Rev. B 78 (2008) 125328.

[11] M. Czerner, M. Bachmann, C. Heiliger, Spin caloritronics in magnetic tunnel junctions: Ab initio studies, Phys. Rev. B 83 (2011) 132405.

[12] N. Liebing, S. Serrano-Guisan, K. Rott, G. Reiss, J. Langer, B. Ocker, H.W. Schumacher, Tunneling Magnetothermopower in Magnetic Tunnel Junction Nanopillars, Phys. Rev. Lett. 107 (2011) 177201.

[13] S. Kolenda, P. Machon, D. Beckmann, W. Belzig, Nonlinear thermoelectric effects in high-field superconductor-ferromagnet tunnel junctions, Beilstein J. Nanotechnol. 7 (2016) 1579.

[14] X.F. Yang, Z.G. Shao, H.L. Yu, Y.J. Dong, Y.W. Kuang, Y.S. Liu, Carbon chain-based spintronic devices: Tunable single-spin Seebeck effect, negative differential resistance and giant rectification effects, Organic Electronics 55 (2018) 170.

[15] M. Hatami, G.E.W. Bauer, Q. Zhang, P.J. Kelly, Thermoelectric effects in magnetic nanostructures, Phys. Rev. B 79 (2009) 174426.

[16] M. Hatami, G.E.W. Bauer, S. Takahashi, S. Maekawa, Thermoelectric spindiffusion in a ferromagnetic metal, Solid State Commun. 150 (2010) 480.

[17] B. Balke, S. Ouardi, T. Graf, J. Barth, C.G.F. Blum, G.H. Fecher, A. Shkabko, A.Weidenkaff, C. Felser, Seebeck coefficients of half-metallic ferromagnets, Solid State Commun. 150 (2010) 529.

[18] A. Kirihara, K.-I. Uchida, Y. Kajiwara, M. Ishida, Y. Nakamura, T. Manako, E. Saitoh, S. Yorozu, Spin-current-driven thermoelectric coating, Nature Mat. 11 (2012) 686.

[19] M.E. Flatté and G. Vignale, Unipolar spin diodes and transistors, Appl. Phys. Lett. 78 (2001) 1273.

[20] C.J. Palmstrøm, Heusler compounds and spintronics, Progr. Cryst. Growth Charac. Mater. 62 (2016) 371.

[21] J. Glanz, Making a Bigger Chill With Magnets, Science 279 (1998) 2045.

[22] K.A. Gschneidner, V. K. Pecharsky, and A. O. Tsokol, Recent developments in magnetocaloric materials, Rep. Prog. Phys. 68 (2005) 1479.

[23] X. Si, Y. Liu, W. Lei, J. Xu, W. Du, J. Lin, T. Zhou, X. Lu, Enhancement of Curie temperature and transition temperature range induced by Al doping in$Mn_{1-x}Al_xCoGe$, Solid State Commun. 247 (2016) 27.

[24] M.V. Costache, G. Bridoux, I. Neumann, S.O. Valenzuela, Magnon-drag thermopile, Nature Materials 11 (2012) 199.

[25] S. Sze, VLSI Technology, McGraw-Hill Book Co., New York, 1988.

[26] C. Zeng, S.C. Erwin, L.C. Feldman, A.P. Li, R. Jin, Y. Song, J.R. Thompson, H.H. Weitering, Epitaxial ferromagnetic Mn_5Ge_3 on Ge(111), Appl. Phys. Lett., Vol. 83 (2003) 5002.

[27] O. Abbes, A. Portavoce, V. Le Thanh, C. Girardeaux, L. Michez, Phase formationduring Mn thin film reaction with Ge: self-aligned germanide process forspintronics, Appl. Phys. Lett. 103 (2013) 172405.

[28] I.A. Fischer, J. Gebauer, E. Rolseth, P. Winkel, L.-T. Chang, K.L. Wang, C. Sürgers, J. Schulze, Ferromagnetic $Mn_5Ge_3C_{0.8}$ contacts on Ge: work function and specific contact resistivity, Semicond. Sci. Technol. 28 (2013) 125002.

[29] L.-A. Michez, F. Virot, M. Petit, R. Hayn, L. Notin, O. Fruchart, V. Heresanu, M. Jamet, and V. Le Thanh, Magnetic anisotropy and magnetic domain structure in C-doped Mn_5Ge_3, Journal of Applied Physics 118 (2015) 043906.

[30] E. Assaf, A. Portavoce, K. Hoummada, M. Bertoglio, S. Bertaina, High Curie temperature Mn_5Ge_3 thin films produced by non-diffusive reaction, Appl. Phys. Lett. 110 (2017) 072408.

[31] A. Portavoce, E. Assaf, C. Alvarez, M. Bertoglio, R. Clérac, K. Hoummada, C. Alfonso, A. Charaï, O. Pilone, K. Hahn, V. Dolocan, S. Bertaina, Ferromagnetic MnCoGe thin films produced via magnetron sputtering and non-diffusive reaction, Applied Surface Science 437 (2018) 336.

[32] I.A. Fischer, L.-T. Chang, C. Sürgers, E. Rolseth, S. Reiter, S. Stefanov, S. Chiussi, J. Tang, K.L. Wang, J. Schulze, Hanle-effect measurements of spin injection from $Mn_5Ge_3C_{0.8}/Al_2O_3$-contacts into degenerately doped Ge channels on Si, Applied Physics Letters 105 (2014) 222408.

[33] J.P. Gambino, E.G. Colgan, Silicides and ohmic contacts, Materials Chemistry and Physics 52 (1998) 99.

[34] J.A. Kittl, K. Opsomer, C. Torregiani, C. Demeurisse, S. Mertens, D.P. Brunco, M.J.H. Van Dal, A. Lauwers, Silicides and germanides for nano-CMOS applications, Materials Science and Engineering B 154–155 (2008) 144.

[35] A. De Luca, A. Portavoce, M. Texier, N. Burle, D. Mangelinck, G. Isella, First stages of Ni reaction with the Si(Ge) alloy, Journal of Alloys and Compounds 695 (2017) 2799.

[36] L. Bainsla, M. Manivel Raja, A.K. Nigam, K.G. Suresh, CoRuFeX (X = Si and Ge) Heusler alloys: High T_C materials for spintronic applications, Journal of Alloys and Compounds 651 (2015) 631.

[37] F. Bottegoni, C. Zucchetti, S. Dal Conte, J. Frigerio, E. Carpene, C. Vergnaud, M. Jamet, G. Isella, F. Ciccacci, G. Cerullo, and M. Finazzi, Spin-Hall Voltage over a Large Length Scale in Bulk Germanium, Phys. Rev. Lett. 118 (2017) 167402.

[38] M. Gajdzik, C. Sürgers, M.T. Kelemen, H.v. Löhneysen, Strongly enhanced Curie temperature in carbon-doped Mn_5Ge_3 films, Journal of Magnetism and Magnetic Materials 221 (2000) 248.

[39] N.T. Trung, L. Zhang, L. Caron, K.H.J. Buschow, E. Brück, Giant magnetocaloriceffects by tailoring the phase transitions, Appl. Phys. Lett. 96 (2010) 172504.

[40] N.T. Trung, V. Biharie, L. Zhang, L. Caron, K.H.J. Buschow, E. Brück, Fromsingle-to double-first-order magnetic phase transition in magnetocaloric $Mn_{1-x}Cr_xCoGe$ compounds, Appl. Phys. Lett. 96 (2010) 162507.

[41] G.J. Li, E.K. Liu, H.J. Zhang, Y.J. Zhang, J.L. Chen, W.H. Wang, H.W. Zhang, G.H.Wu, S.Y. Yu, Phase diagram, ferromagnetic martensitic transformation and Magnetoresponsive properties of Fe-doped MnCoGe alloys, J. Magn. Magn. Mater. 332 (2013) 146.

[42] E.K. Liu, W.Z., L. Feng, J.L. Chen, W.H. Wang, G.H. Wu, H.Y. Liu, F.B. Meng, H.Z. Luo, Y.X. Li, Vacancy-tuned paramagnetic/ferromagnetic martensitic transformation in Mn-poor $Mn_{1-x}CoGe$ alloys. A letters journal exploring the frontiers of physics 91 (2010) 17003.

[43] W.D.-H. Ma Sheng-Can, X. Hai-Cheng, S. Ling-Jia, C. Qing-Qi, D. You-Wei, Effects of the Mn/Co ratio on the magnetic transition and magnetocaloric properties of $Mn_{1+x}Co_{1-x}Ge$ alloys. Chin. Phys. B 20 (2011) 087502.

[44] Z. Gercsi, K.H., and K.G. Sandeman, Designed metamagnetism in $CoMnGe_{1-x}P_x$. Phys. Rev. B 83 (2011) 174403.

[45] J.B.A. Hamer, S. Ozcan, N.D. Mathur, D.J. Fray, K.G. Sandeman, Phase diagram and magnetocaloric effect of $CoMnGe_{1-x}Sn_x$ alloys. Journal of Magnetism and Magnetic Materials 321 (2009) 3535.

[46] X. Si, Y. Shen, X. Ma, S. Chen, J. Lin, J. Yang, T. Gao, Y. Liu, Field dependence of magnetic entropy change and estimation of spontaneous magnetization in Cd substituted MnCoGe, Acta Materialia, 143 (2018) 306.

[47] X. Si, Y. Liu, Y. Shen, W. Yu, X. Ma, Z. Zhang, Y. Xu, T. Gao, Critical behavior and magnetocaloric effect near room temperature in $MnCo_{1-x}Ti_xGe$ alloys, Intermetallics 93 (2018) 30.

[48] X. Si, Y. Liu, X. Ma, J. Lin, J. Yang, T. Zhou, The analysis of magnetic entropy change and long-range ferromagnetic order in $Mn_{1-x}Ag_xCoGe$, J. Mater. Sci. 54 (2019) 3196.

[49] L. Caron, N.T. Trung, E. Brück, Pressure-tuned magnetocaloric effect in $Mn_{0.93}Cr_{0.07}CoGe$. Phys. Rev. B 84 (2011) 020414.

[50] S. Niziol, R. Zach, J.P. Senateur, J. Beille, pressure dependence of the magnetic transition temperature of the $CoMnGe_{1-x}Si_x$ system. Journal of Magnetism and Magnetic Materials 79 (1989) 333.

[51] Y.W. Li, H. Zhang, K. Tao, Y.X. Wang, M.L. Wu, Y. Long, Giant magnetocaloric effect induced by reemergence of magnetostructural coupling in Si-doped $Mn_{0.95}CoGe$ compounds, Materials and Design 114 (2017) 410.

[52] L.F. Bao, F.X. Hu, R.R. Wu, J. Wang, L. Chen, J.R. Sun, B.G. Shen, L. Li, B. Zhang, X.X. Zhang, Evolution of magnetostructural transition and magnetocaloric effect with Al doping in $MnCoGe_{1-x}Al_x$ compounds. Journal of Physics D: Applied Physics 47 (2014) 055003.

[53] T. Samanta, I. Dubenko, A. Quetz, S. Stadler, N. Ali, Giant magnetocaloric effects near room temperature in $Mn_{1-x}Cu_xCoGe$, Applied Physics Letters 101 (2012) 242405.

[54] S. Salomon, S. Hamann, P. Decker, A. Savan, L. Meshi, A. Ludwig, Combinatorial synthesis and high-throughput characterization of the thin film materials system Co-Mn–Ge: Composition, structure, and magnetic properties, Phys. Status Solidi A 212 (2015) 1969.

[55] Y. Liu, K.M. Qiao, S.L. Zuo, H.R. Zhang, H. Kuang, J. Wang, F.X. Hu, J.R. Sun, B.G. Shen, Negative thermal expansion and magnetocaloric effect in Mn-Co-Ge-In thin films, Appl. Phys. Lett. 112 (2018) 012401.

[56] B.T. Massalski, H. Okamoto, P.R. Subramanian, L. Kacprzak, Binary Alloy Phase Diagrams, ASM International, 1996.

[57] P. Stadelmann, EMS - a software package for electron diffraction analysis and HREM image simulation in materials science, Ultramicroscopy 21 (1987) 131.

[58] J.M. Cowley and A.F. Moodie, The scattering of electrons by atoms and crystals. I. A new theoretical approach, Acta. Cryst. 10 (1957) 609.

[59] C. Jing, S.X. Cao, J. C. Zhang, Lattice constant dependence of magnetic properties in bcc and fcc Fe_xMn_{1-x} alloys, Phys. Rev. B 68 (2003) 224407.

[60] A.R. Denton and N.W. Ashcroft, Vegard's law, Phys. Rev. A 43 (1991) 3161.

[61] W. Knaepen, S. Gaudet, C. Detavernier, R.L. Van Meirhaeghe, J. Jordan Sweet, C. Lavoie, In situ x-ray diffraction study of metal induced crystallization of amorphous germanium, J. Appl. Phys. 105 (2009) 083532.

[62] K. De Keyser, R.L. Van Meirhaeghe, C. Detavernier, J. Jordan-Sweet, C. Lavoie, Texture of Cobalt Germanides on Ge(100) and Ge(111) and its Influence on the Formation Temperature, Journal of The Electrochemical Society 157 (2010) H395.

[63] J. Perrin Toinin, K. Hoummada, M. Bertoglio, A. Portavoce, Origin of the first-phase selection during thin film reactive diffusion: Experimental and theoretical insights into the Pd-Ge system, Scripta Materialia 122 (2016) 22.

[64] K.R. Hahn, E. Assaf, A. Portavoce, S. Bertaina, A. Charaï, Structural and Composition Effects on Electronic and Magnetic Properties in Thermoelectric $Mn_{1-x-y}Co_{1+x}Ge_{1+y}$ Materials, J. Phys. Chem. C 121 (2017) 26575.

[65] E.K. Liu, W. Zhu, L. Feng, J.L. Chen, W.H. Wang, G.H. Wu, H.Y. Liu, F.B. Meng,H.Z. Luo, Y.X. Li, Vacancy-tuned paramagnetic/ferromagnetic martensitic transformation in Mn-poor $Mn_{1-x}CoGe$ alloys, EPL 91 (2010) 17003.

[66] R. Jean-Jacques and G. Alain, Cristallographie géométrique et radiocristallographie, Dunod, Paris, 2007.

[67] ICDD. International Centre for Diffraction Data. Available from: http://www.icdd.com/.

[68] C. Rivero, P. Gergaud, O. Thomas, B Froment, H. Jaouen, In situ study of stress evolution during the reaction of a nickel film with a silicon substrate, Microelectronic Engineering 76 (2004) 318.

[69] H. Mehrer, Diffusion in Solids, Springer-Verlag, Berlin, Heidelberg, 2007.

[70] S. Kaprzyk and S. Niziol, The electronic structure of CoMnGe with the hexagonal and orthorhombic crystal structure, J. Magnetism and Magnetic Materials 87 (1990) 267.

[71] Y. Yan, S.J. Pennycook, Z. Xu, D. Viehland, Determination of the ordered structures of $Pb(Mg_{1/3}Nb_{2/3})O_3$ and $Ba(Mg_{1/3}Nb_{2/3})O_3$ by atomic-resolution Z-contrast imaging, Appl. Phys. Lett. 72 (1998) 3145.

[72] Y. Fujino, D. Shinoda, S. Asanabe, Y. Sasaki, Phase diagram of the partial system of MnSi-Si, Jap. J. Appl. Phys. 3 (1964) 431.

[73] O. Schwomma, H. Nowotny, A. Wittmann, Die Kristallarten $RuSi_{1,5}$, $RuGe_{1,5}$ und $MnSi_{\sim 1,7}$, Monatsh. Chem. 94 (1963) 681.

[74] O. Schwomma, A. Presinger, H. Nowotny, A. Wittmann, Kristall Structure von $Mn_{11}Si_{19}$ und deren Zusammenhang mit Disilicid, Monatsh. Chem. 95 (1964) 1527.

[75] H.W. Knott, M.H. Mueller, L. Heaton, The Crystal structure of $Mn_{15}Si_{26}$, Acta Cryst. 23 (1967) 549.

[76] H. Nowotny, The Chemistry of Extended Defects in Non-Metallic Solids, Ed. Le Roy Eyring and M. O'Keefe, North-Holland Publ. Co., Amsterdam, 1970.

[77] A. Portavoce and K. Hoummada, Role of Atomic Transport Kinetic on Nano-Film Solid State Growth, Diffusion in High-tech Materials, Diffusion Foundations 17 (2018) 115, Ed. H. Mehrer, Trans Tech Publications, Switzerland, 2018.

[78] F. Guillou, F. Wilhelm, O. Tegus, A. Rogalev, Microscopic mechanism of the giant magnetocaloric effect in MnCoGe alloys probed by x-ray magnetic circular dichroism, Appl. Phys. Lett. 108 (2016) 122405.

[79] J. Zeng, Z. Wang, Z. Nie, Y. Wang, Crystal structural transformation accompanied by magnetic transition in $MnCo_{1-x}Fe_xGe$ alloys, Intermetallics 52 (2014) 101.

[80] S. Nizioł, A. Wesełucha, W. Bazela, A. Szytuła, Magnetic properties of the $Co_xNi_{1-x}MnGe$ system, Solid State Communications 39 (1981) 1081.

[81] Z. Wang, Z. Nie, J. Zeng, R. Su, Y. Zhang, D.E. Brown, Y. Ren, Y. Wang, First-order magnetostructural transformation in Fe doped Mn–Co–Ge alloys, Journal of Alloys and Compounds 577 (2013) 486.

[82] W. Platow, A.N. Anisimov, G.L. Dunifer, M. Farle, K. Baberschke, Phys. Rev. B 58 (1998) 5611.

[83] C.-E. Dutoit, V.O. Dolocan, M. Kuzmin, L. Michez, M. Petit, V. Le Thanh, B. Pigeau, S. Bertaina, J. Phys. D: Appl. Phys. 49 (2016) 045001.

[84] C. Chappert, K. Le Dang, P. Beauvillain, H. Hurdequint, D. Renard, Ferromagnetic resonance studies of very thin cobalt films on a gold substrate, Phys. Rev. B 34 (1986) 3192.

FIGURE CAPTIONS

FIG. 1. X-ray diffractograms ($20° \leq 2\theta \leq 60°$) acquired at different temperatures during *in situ* thermal annealing from 323 to 673 K using an average heating ramp of 1 K/min: a) Mn/Co sample, b) Mn/Ge sample, and c) Co/Ge sample.

FIG. 2. AFM measurements performed on the surface of the Co/Ge/Mn sample a) before and b) after annealing.

FIG. 3. X-ray diffractograms ($20° \leq 2\theta \leq 60°$) acquired at different temperatures during *in situ* thermal annealing of the Co/Ge/Mn sample, using an average heating ramp of 1 K/min from 323 to 673 K (a), followed by an isothermal annealing at 673 K for 3 days (b).

FIG. 4. Variations of normalized and integrated XRD peak intensities recorded during in situ annealing of the Co/Ge/Mn sample as a function of the XRD scan number: scan 1 to 71 for ramp annealing (1K/min) from 323 to 675 K, scan 72 to 288 for isothermal annealing at 675 K for 3 days. Each peak is labeled with a number corresponding to the peaks' order of appearance. The peaks corresponding to the Mn-Ge reaction (Mn(330), 1-Mn_5Ge_3(112), 4-$Mn_{11}Ge_8$(420), and 6-Mn_5Ge_2(402)) are shown in (a), while the peaks corresponding to the Co-Ge reaction (Co(111), 2-CoGe(020), and 3-$CoGe_2$(204)) are shown in (b). The peaks 5 and 7 correspond respectively to Hexa-MnCoGe(102) and Ortho-MnCoGe(113), and are reported in both (a) and (b).

FIG. 5. X-ray diffractograms acquired during the *in situ* annealing of Co/Ge/Mn sample, the diffractogram #1 was obtained when Hexa-MnCoGe was first detected (60 min at T = 673 K), the

difractogram #2 was measured at the end of the annealing (3 days at T = 673 K), and the diffractogram #3 was acquired at the end of the experiment once the sample was cooled down to RT. Solid triangles correspond to diffraction peaks from Hexa-MnCoGe, and solid stars correspond to diffraction peaks from Ortho-MnCoGe.

FIG. 6. Cross-sectional TEM bright field images acquired on the annealed Co/Ge/Mn sample. These three images illustrate the inhomogeneity of the 20 nm-thick Mn_xSi_y interfacial layer located between the Si substrate and the film.

FIG. 7. Cross-sectional TEM bright field images of the annealed film showing Hexa-MnCoGe (a), Ortho-MnCoGe (b) and mono-CoGe (c) grains, and corresponding power spectra (d-f) recorded from the HREM images. (g – i) show calculated ED patterns.

FIG. 8. Cross-sectional ADF-STEM image (a), EDS profile lines (b) and chemical maps (c) showing the film chemical inhomogeneity.

FIG. 9. Schematic depicting the phase formation sequence occurring during Co/Ge/Mn reactive diffusion.

FIG. 10. (a) Cross-sectional STEM–HAADF image (left) associated with a bright field image (right) corresponding to the area in white rectangular frame. The white square frame shows 2 layers of Mn_xSi_y. (b) HREM image recorded in the Si substrate-first layer of Mn_xSi_y. (c) HREM image recorded in the Mn_xSi_y second layer. The white circles in the power spectra surround the reflections of the Si structure. The red triangle surrounds the (200) reflection of both $Mn_{11}Si_{19}$

and $Mn_{27}Si_{47}$ in the direction $\boldsymbol{a}^*$, and the red square surrounds the (004) reflection of $Mn_{11}Si_{19}$ in the direction $\boldsymbol{c}^*$. The white lines point to reflections separated by 12 Å along $\boldsymbol{c}^*$.

FIG. 11. Magnetic measurements performed in the plane of the MnCoGe film (a) magnetization T-dependence under a magnetic field of 1 T; (b) AC susceptibility measurements showing the in-phase (χ') and out-of-phase (χ'') components; (c) FC and ZFC magnetization curves as a function of $300 \leq T \leq 380$ K measured under a low magnetic field of 10^{-2} T; and (d) magnetic hysteresis loops measured at $T = 2$ and 250 K.

FIG. 12. FMR measurements performed on the MnCoGe film at $T = 250$ K: (a) FMR signals with in-plane applied magnetic field (black line, $\varphi_H = 0°$) and out-of-plane applied magnetic field (red line, $\varphi_H = 90°$); and (b) angular variations (versus φ_H) of the resonance field H_r. The red solid line corresponds to a simulation using the twofold-anisotropy Chappert model.

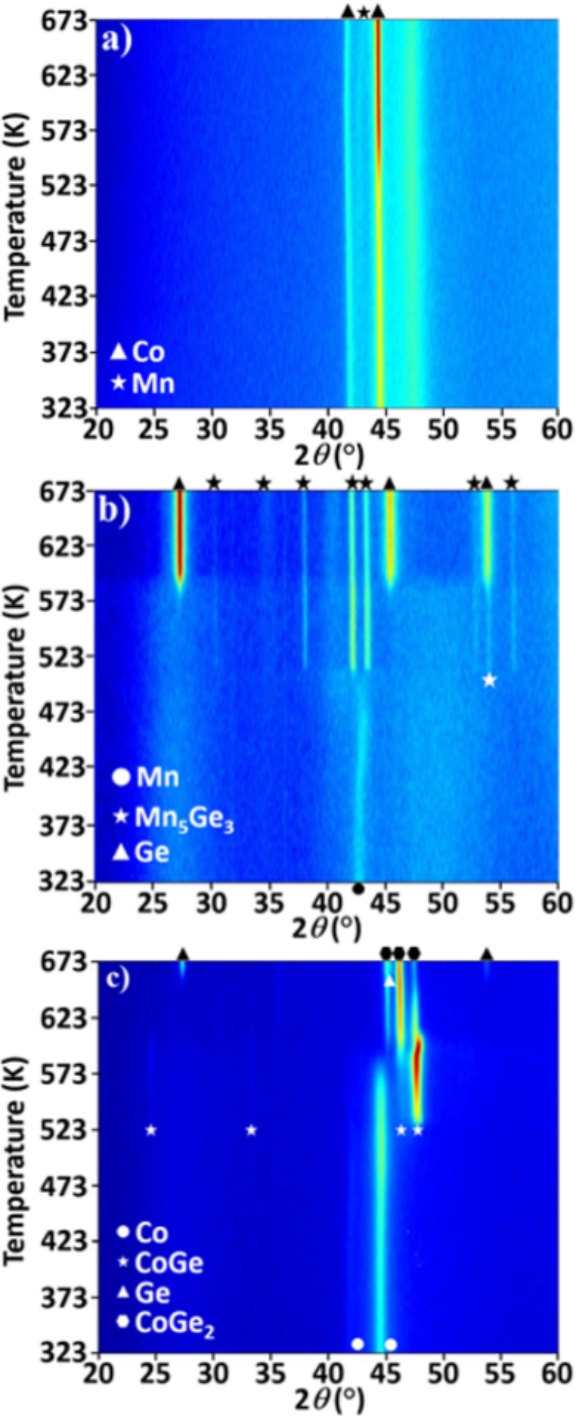
a)
Co
Mn
b)
Mn
Mn_5Ge_3
Ge
c)
Co
CoGe
Ge
$CoGe_2$
Temperature (K)
673
623
573
523
473
423
373
323
20
25
30
35
40
45
50
55
60
2θ(°)

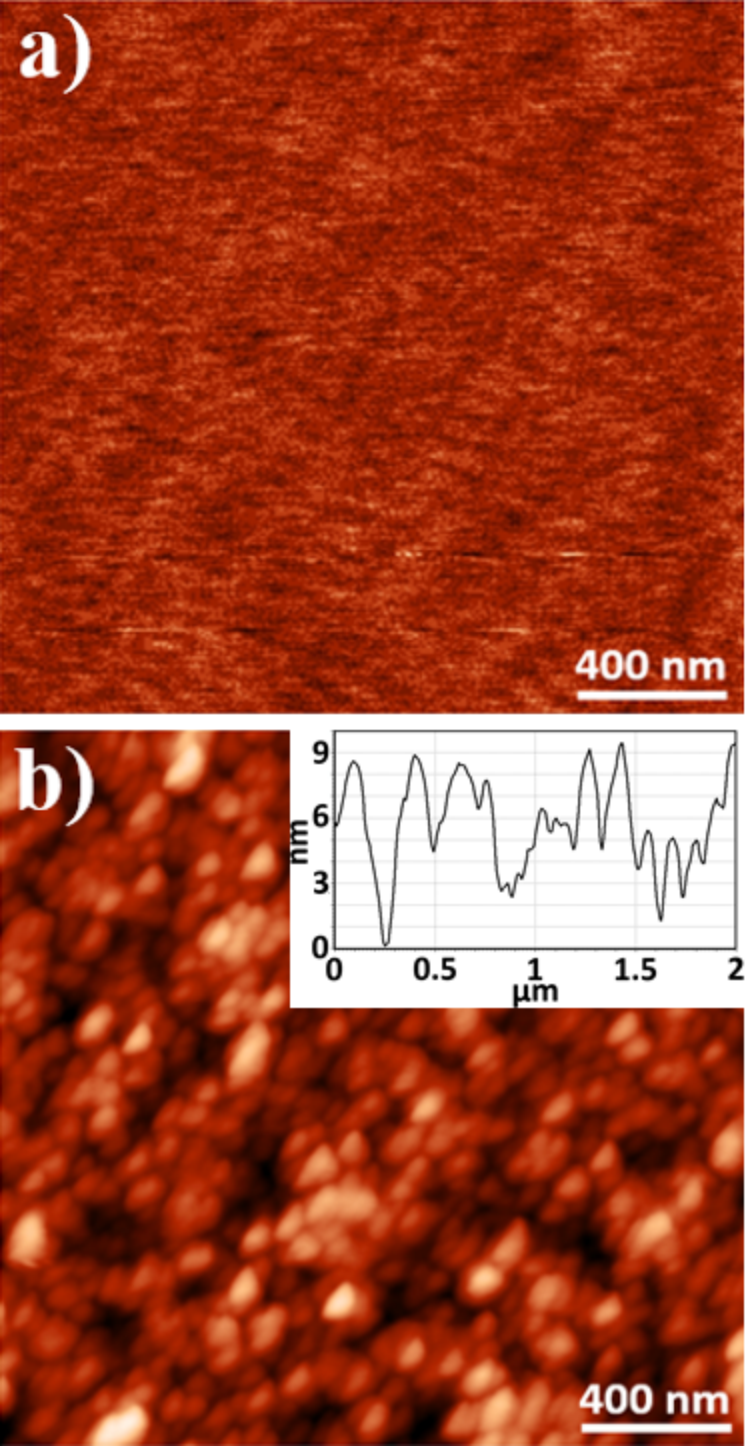
a)
400 nm
b)
nm
9
6
3
0
0
0.5
1
1.5
2
µm
400 nm

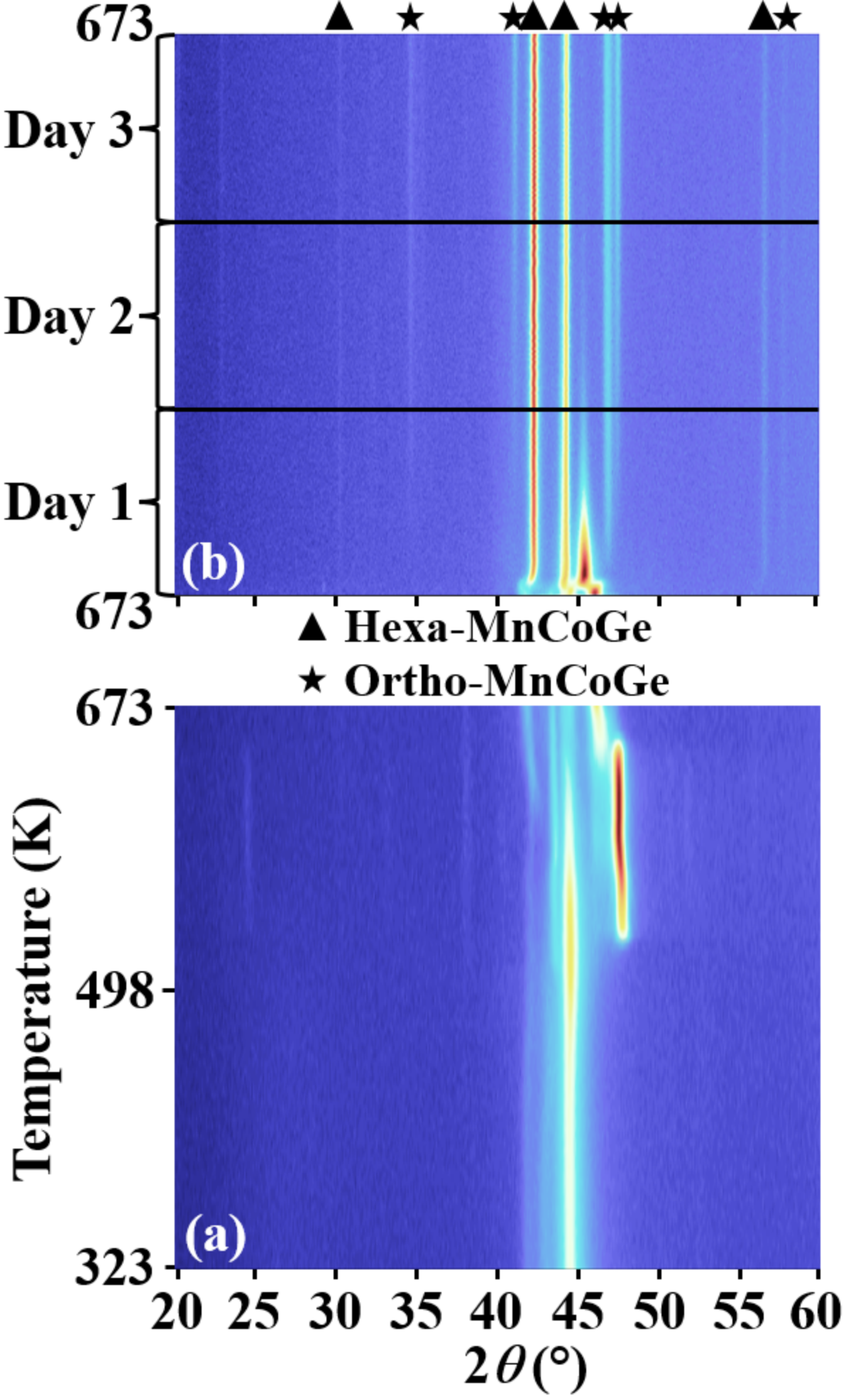
673
Day 3
Day 2
Day 1
(b)
673
▲ Hexa-MnCoGe
★ Ortho-MnCoGe
673
498
323
Temperature (K)
(a)
20 25 30 35 40 45 50 55 60
2θ (°)

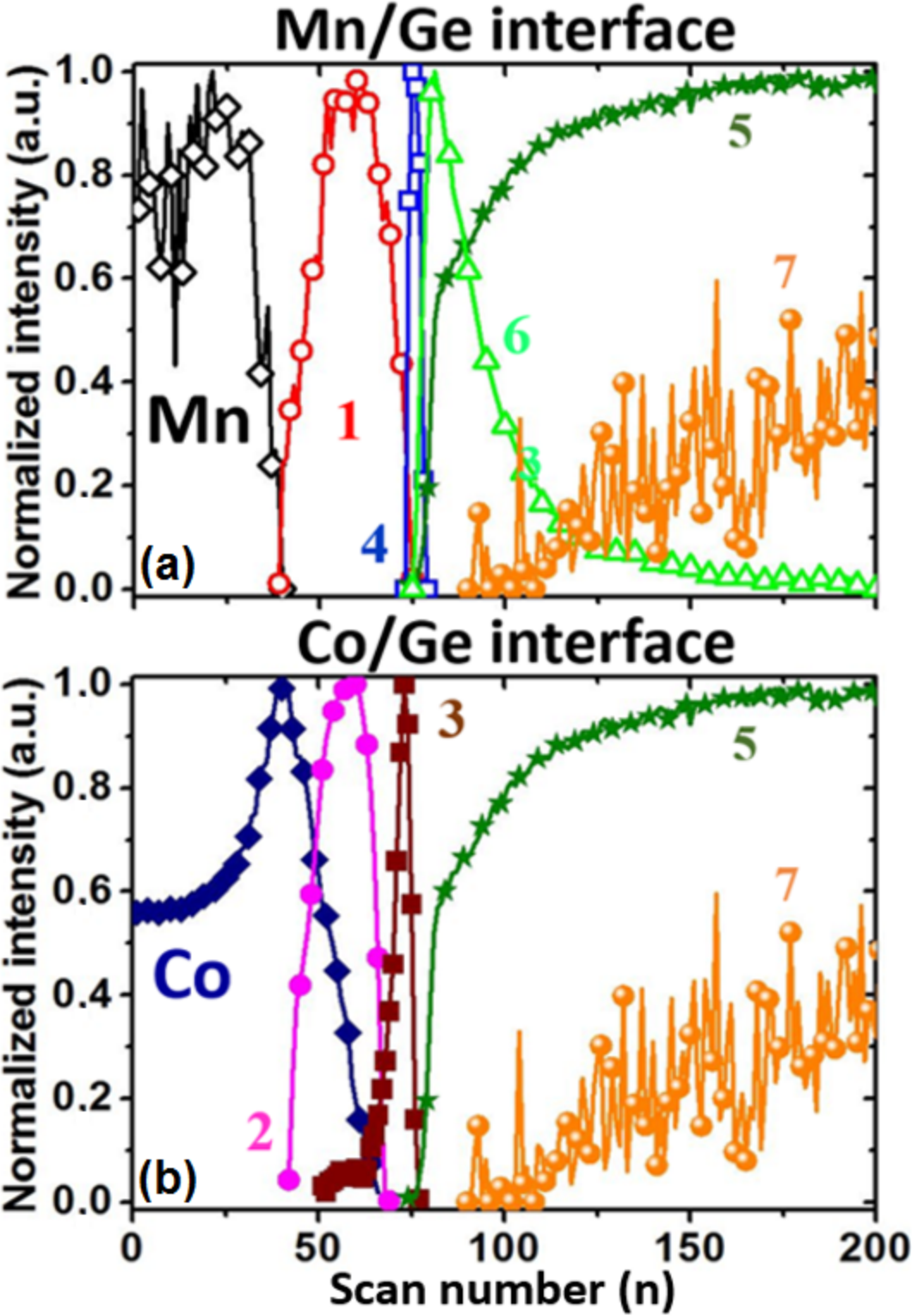
Mn/Ge interface
Normalized intensity (a.u.)
1.0
0.8
0.6
0.4
0.2
0.0
Mn
1
4
6
3
5
7
(a)
Co/Ge interface
Co
2
3
5
7
(b)
0
50
100
150
200
Scan number (n)

▲ Hexa
★ Ortho
1 — 60 min at 673K
2 — 3 days at 673K
3 — After annealing, at RT
Intensity (a.u.)
3
2
1
$Mn_{11}Ge_8$
$CoGe_2$
40 41 42 43 44 45 46 47 48 49
2θ(°)

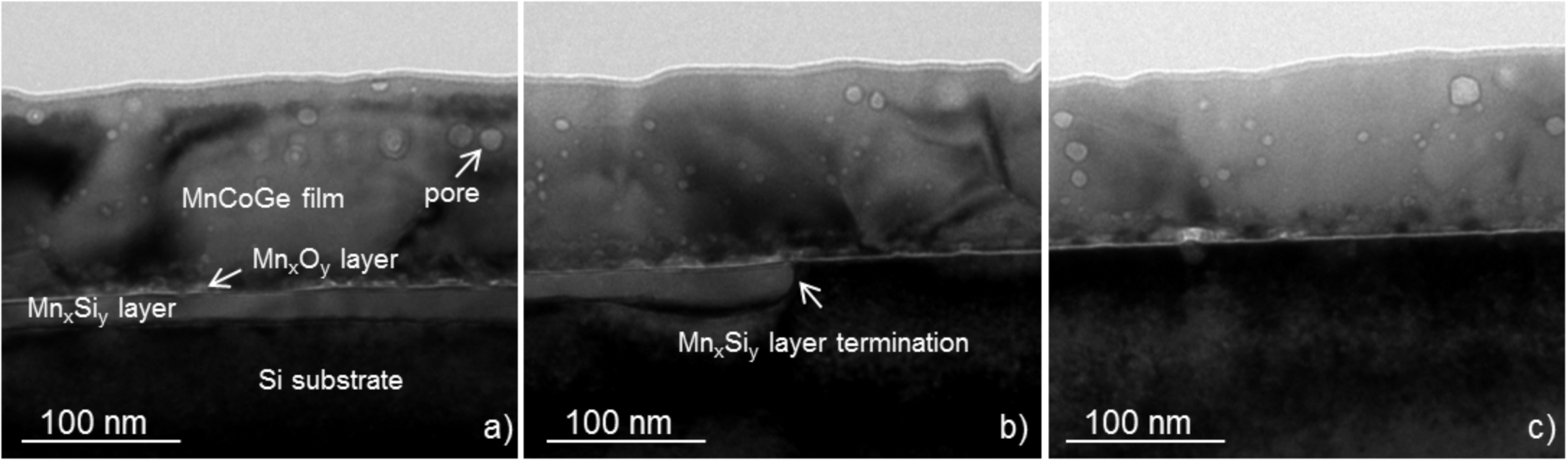
MnCoGe film
pore
Mn_xO_y layer
Mn_xSi_y layer
Si substrate
100 nm
a)
Mn_xSi_y layer termination
100 nm
b)
100 nm
c)

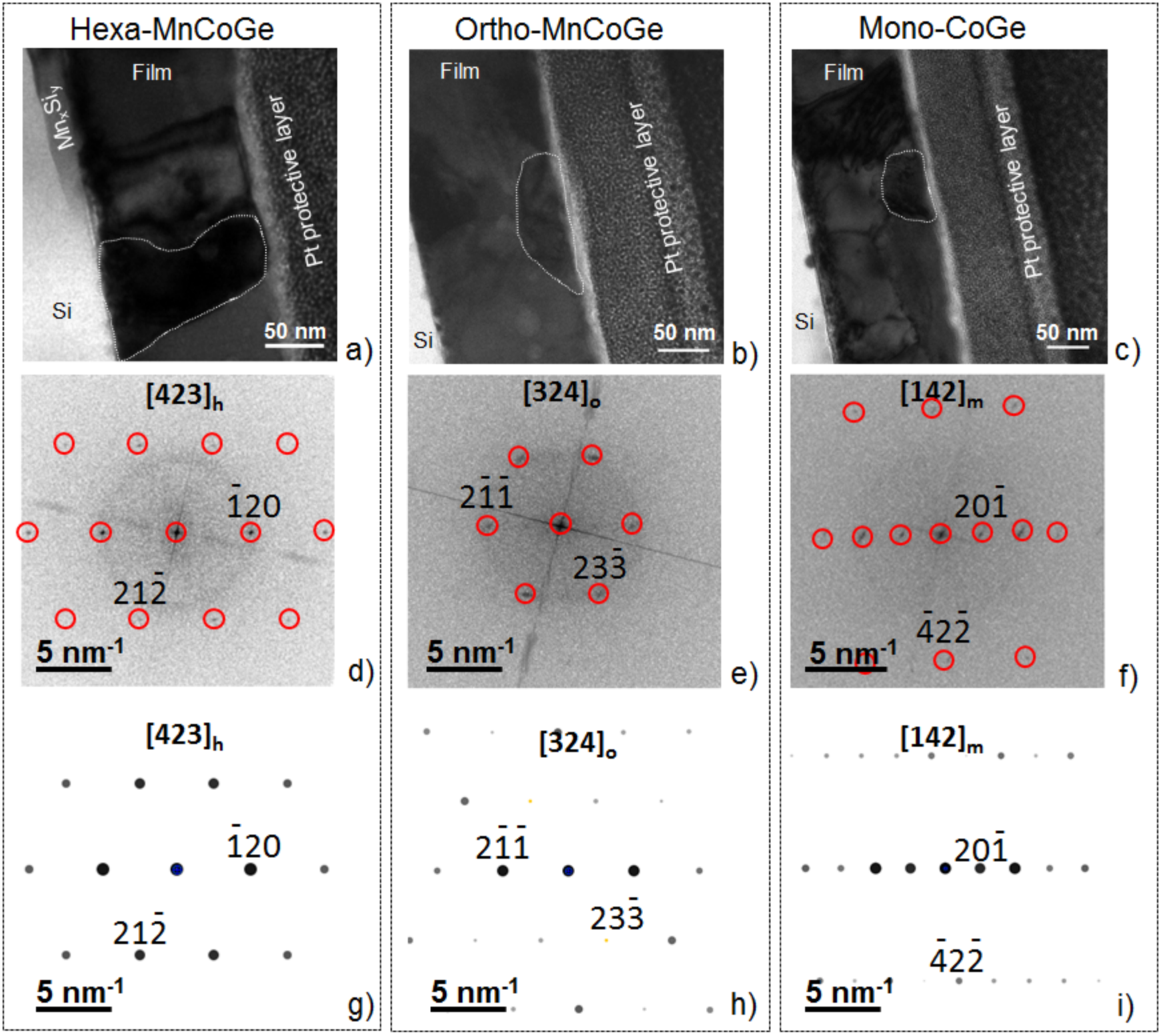
Hexa-MnCoGe
Ortho-MnCoGe
Mono-CoGe
Film
Mn_xSi_y
Pt protective layer
Si
50 nm
a)
b)
c)
$[423]_h$
$\bar{1}20$
$21\bar{2}$
5 nm^{-1}
d)
$[324]_o$
$2\bar{1}\bar{1}$
$23\bar{3}$
e)
$[142]_m$
$20\bar{1}$
$\bar{4}2\bar{2}$
f)
g)
h)
i)

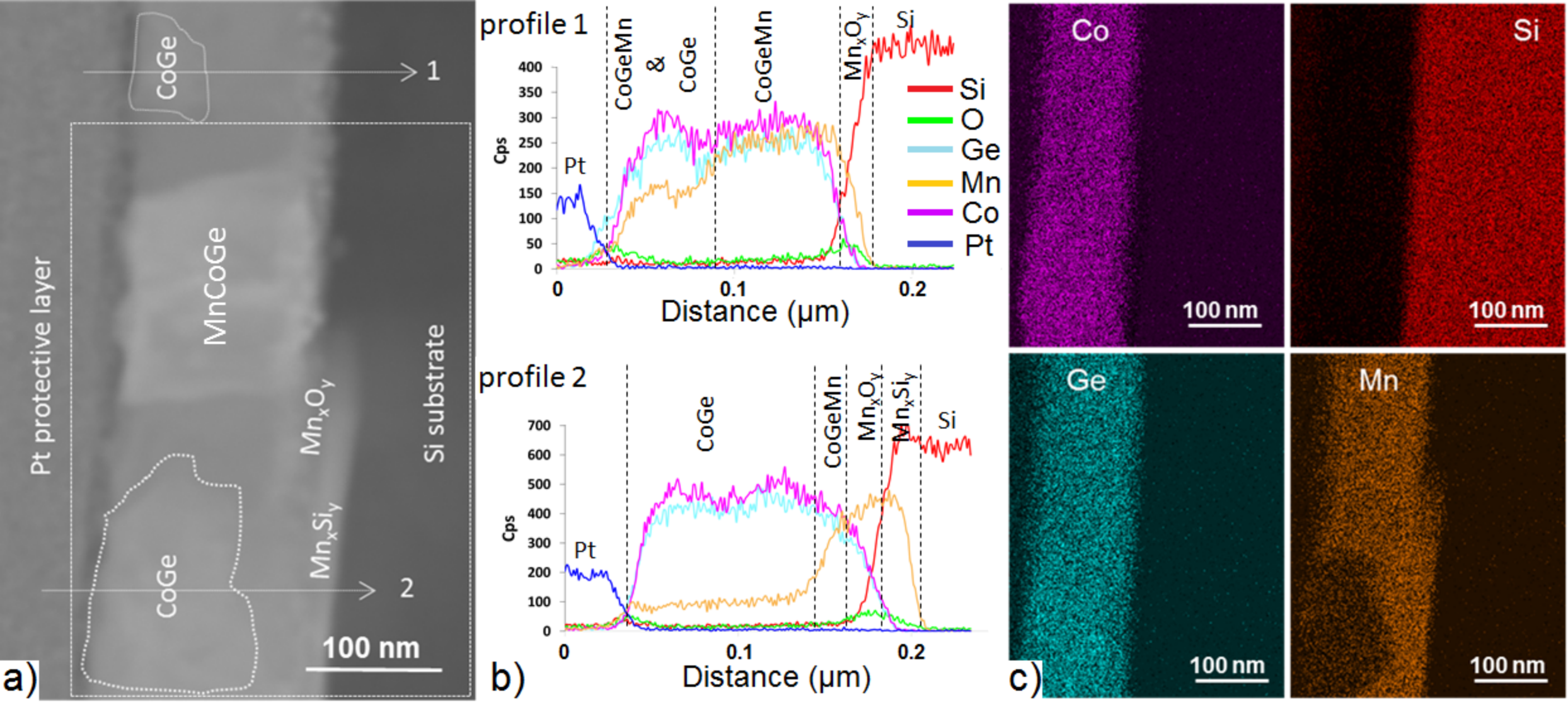
a)
CoGe
1
MnCoGe
Pt protective layer
Si substrate
Mn_xO_y
Mn_xSi_y
CoGe
2
100 nm
b)
profile 1
CoGeMn
&
CoGe
CoGeMn
Mn_xO_y
Si
Pt
Cps
Si
O
Ge
Mn
Co
Pt
Distance (μm)
profile 2
CoGe
CoGeMn
Mn_xO_y
Mn_xSi_y
Si
Pt
Cps
Distance (μm)
c)
Co
Si
Ge
Mn
100 nm

SiO_2

Co | Ge | Mn

T < 673 K

Co | CoGe | Ge | Mn_5Ge_3 | Mn

CoGe | $CoGe_2$ | Ge | Mn_5Ge_3

T = 673 K

CoGe | $CoGe_2$ | Ge | $Mn_{11}Ge_8$ | Mn_5Ge_3

T = 673 K
t = 40 min

CoGe | $CoGe_2$ | $Mn_{11}Ge_8$ | Mn_5Ge_3

CoGe | $CoGe_2$ | Hexa-MnCoGe | Mn_5Ge_3 / $Mn_{11}Ge_8$

T = 673 K
t = 60 min

CoGe | $CoGe_2$ | Hexa-MnCoGe | $Mn_{11}Ge_8$

CoGe | $CoGe_2$ | Hexa-MnCoGe | Mn_5Ge_2 $Mn_{11}Ge_8$

T = 673 K
t = 80 min

CoGe | Hexa-MnCoGe | Mn_5Ge_2

silicide
t = 100 min

CoGe / Ortho-MnCoGe | Hexa-MnCoGe | Mn_5Ge_2

silicide
t = 380 min

CoGe / Ortho-MnCoGe | Hexa-MnCoGe

silicide

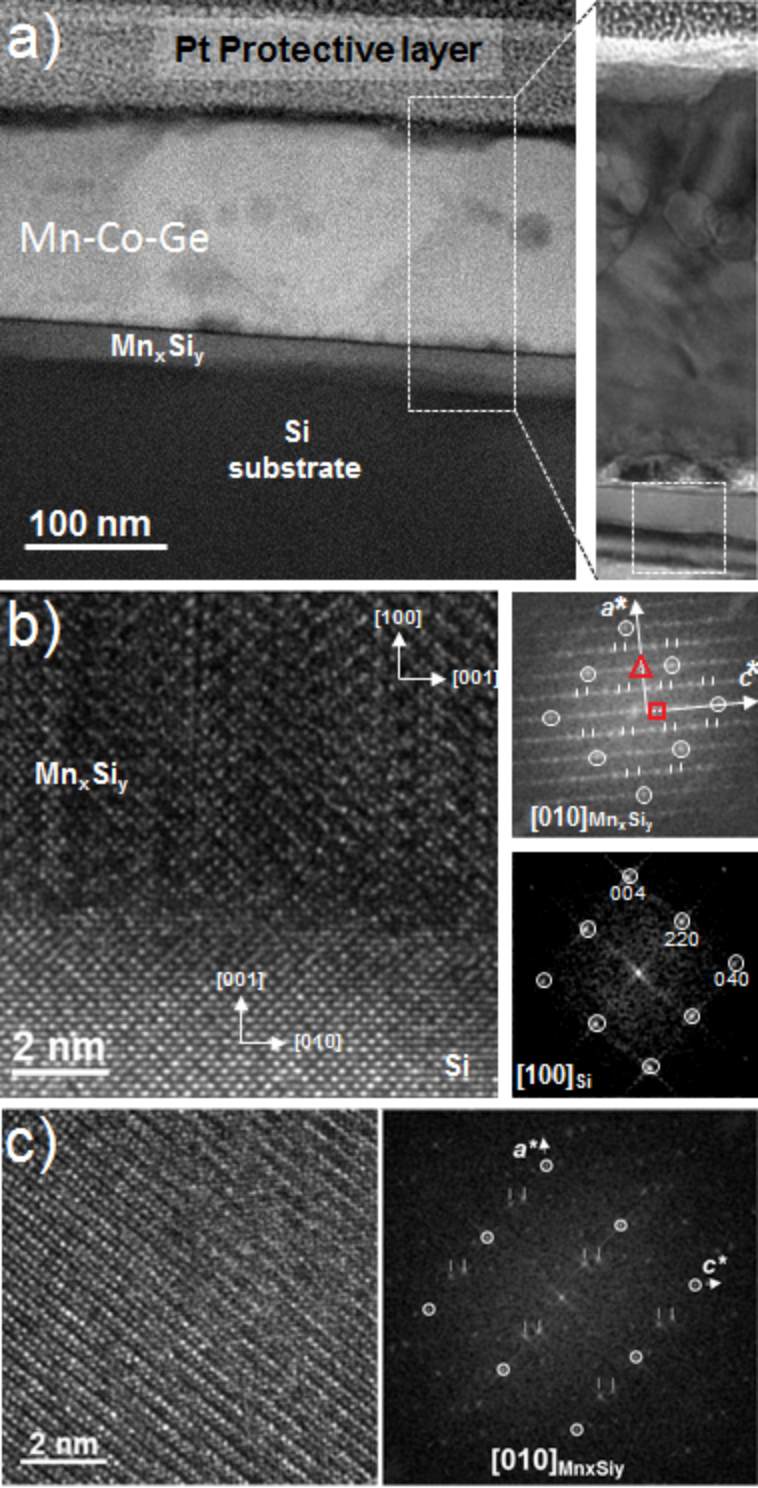
a)
Pt Protective layer
Mn-Co-Ge
Mn_xSi_y
Si
substrate
100 nm
b)
[100]
[001]
Mn_xSi_y
[001]
[010]
2 nm
Si
a*
c*
$[010]_{Mn_xSi_y}$
004
220
040
$[100]_{Si}$
c)
2 nm
a*
c*
$[010]_{MnxSiy}$

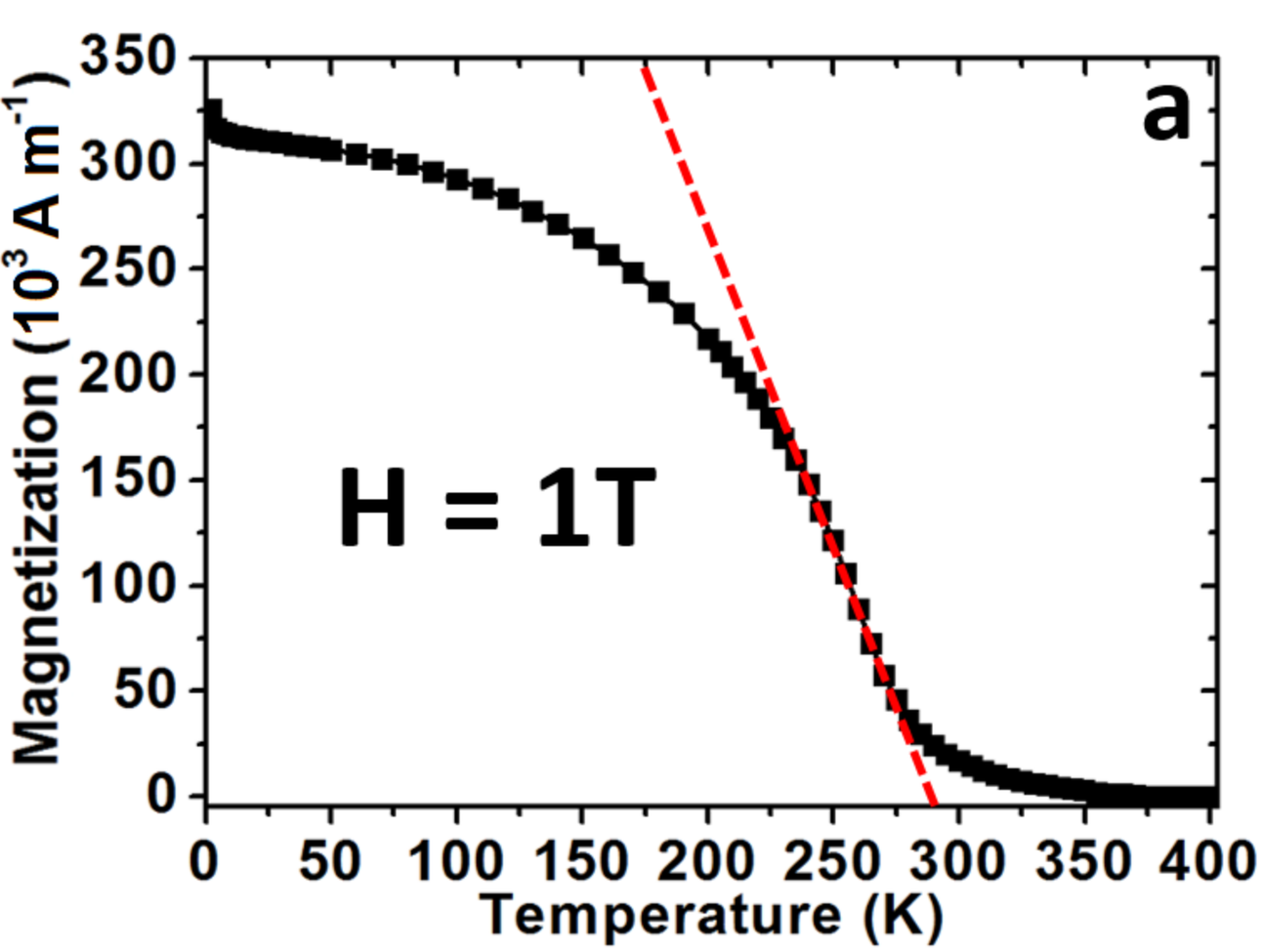
a
H = 1T
Magnetization (10^3 A m^{-1})
Temperature (K)
0
50
100
150
200
250
300
350
400

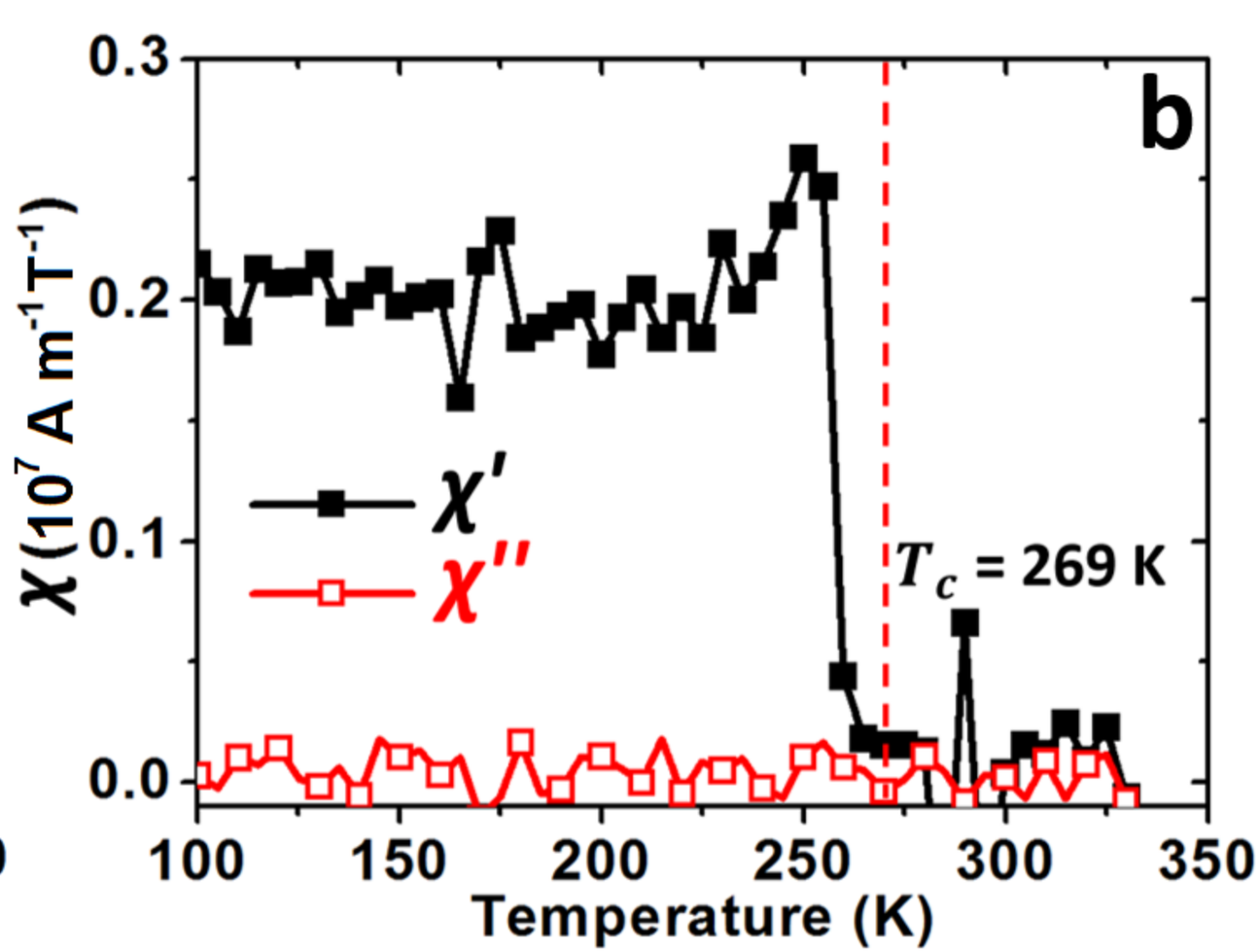
b
χ'
χ''
T_c = 269 K
χ (10^7 A m^{-1}T^{-1})
Temperature (K)
0.0
0.1
0.2
0.3
100
150
200
250
300
350

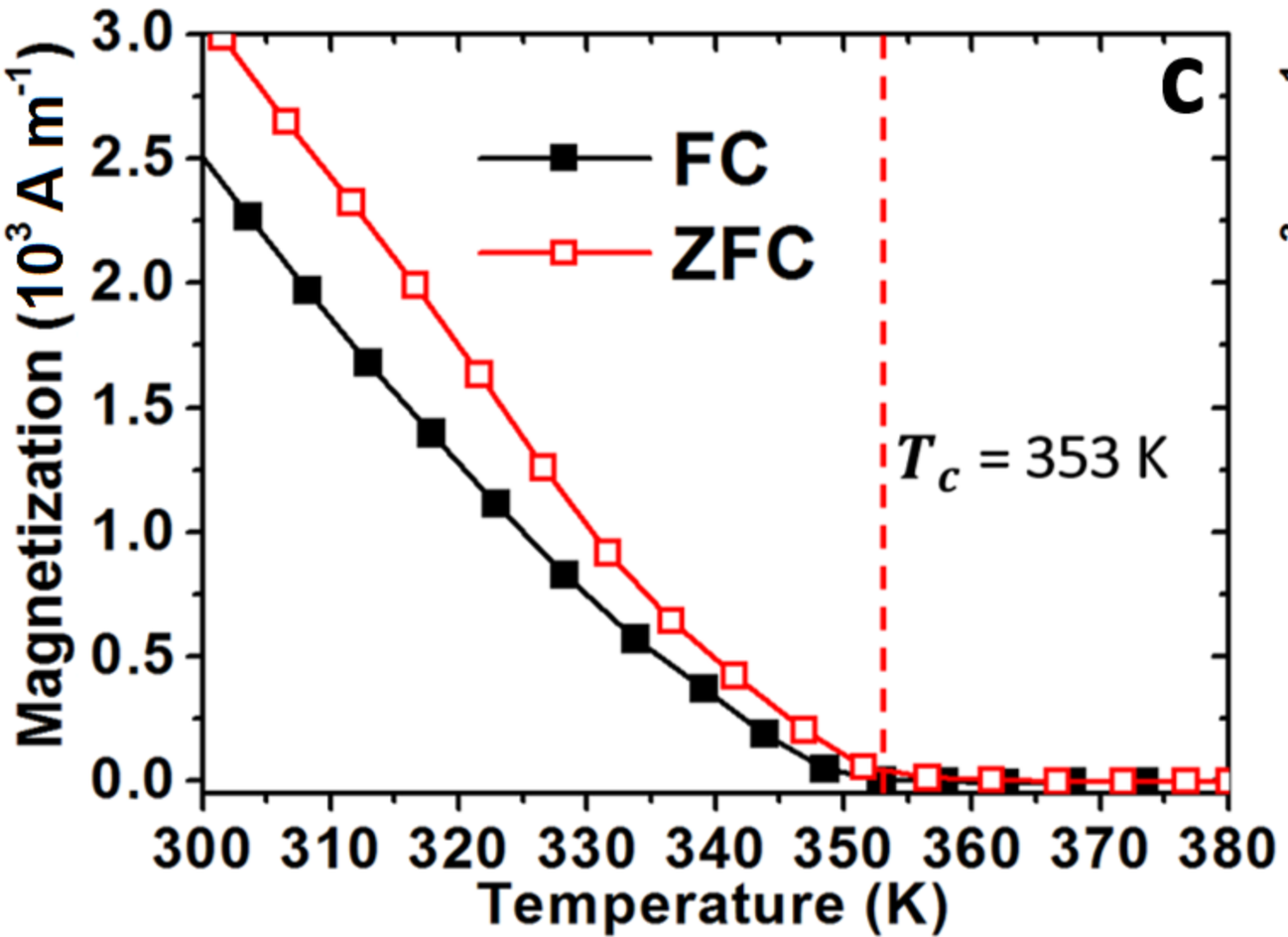
c
FC
ZFC
T_c = 353 K
Magnetization (10^3 A m^{-1})
Temperature (K)
0.0
0.5
1.0
1.5
2.0
2.5
3.0
300
310
320
330
340
350
360
370
380

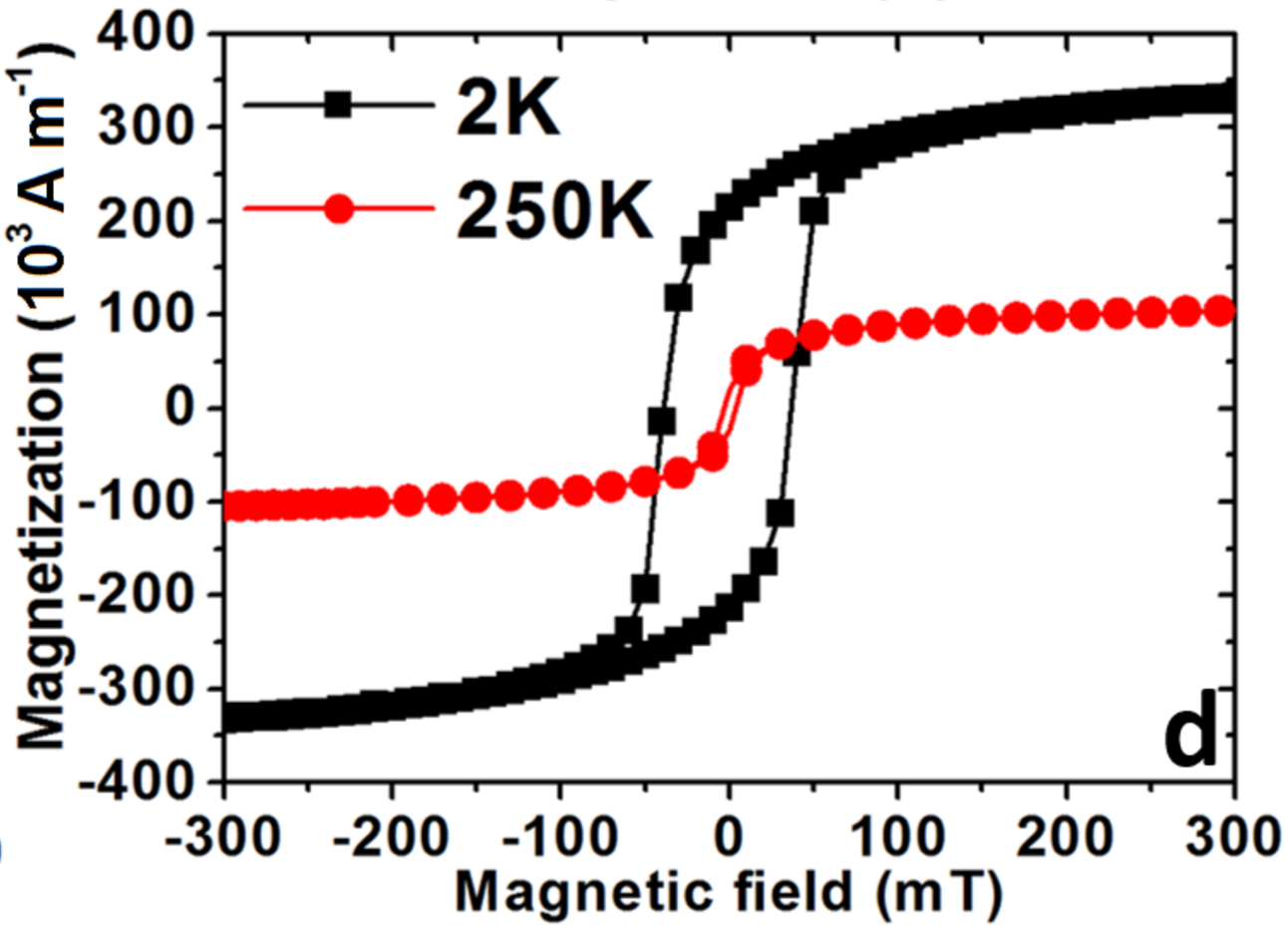
d
2K
250K
Magnetization (10^3 A m^{-1})
Magnetic field (mT)
-400
-300
-200
-100
0
100
200
300
400

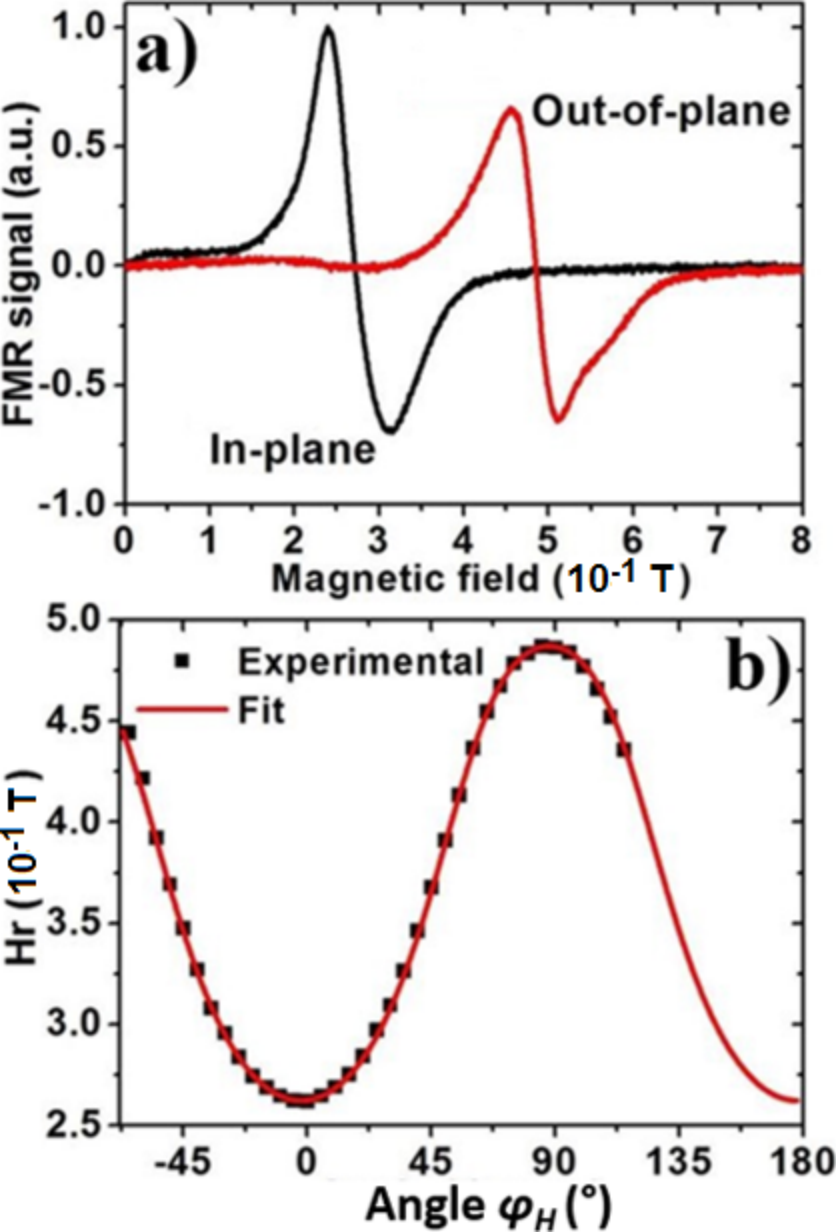
a)
Out-of-plane
In-plane
FMR signal (a.u.)
1.0
0.5
0.0
-0.5
-1.0
0
1
2
3
4
5
6
7
8
Magnetic field (10-1 T)
b)
Experimental
Fit
Hr (10-1 T)
5.0
4.5
4.0
3.5
3.0
2.5
-45
0
45
90
135
180
Angle φH (°)

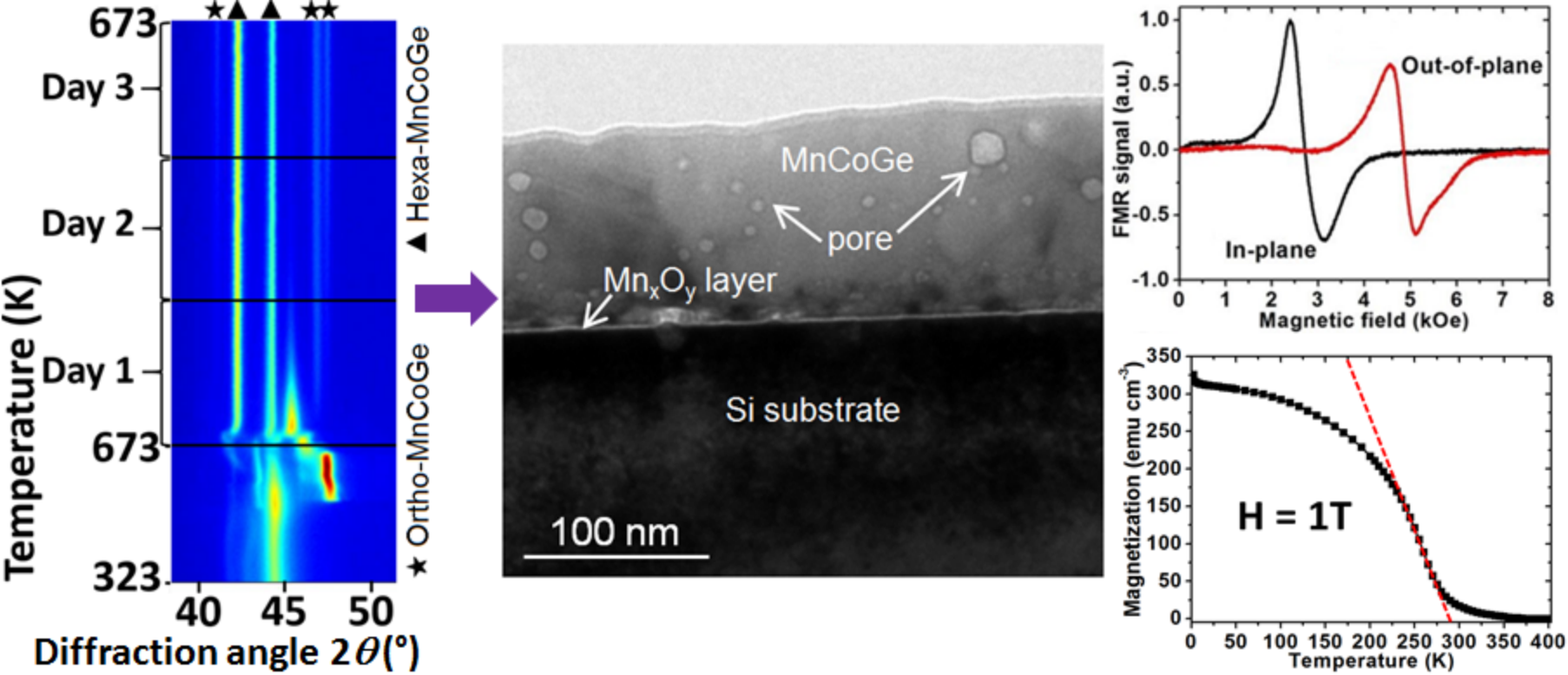
673
Day 3
Day 2
Day 1
673
323
Temperature (K)
40
45
50
Diffraction angle 2θ(°)
▲ Hexa-MnCoGe
★ Ortho-MnCoGe
MnCoGe
pore
MnxOy layer
Si substrate
100 nm
FMR signal (a.u.)
Out-of-plane
In-plane
Magnetic field (kOe)
Magnetization (emu cm-3)
H = 1T
Temperature (K)